Evaluating landslide response in seismic and rainfall regime: A case study from the SE Carpathians, Romania

[1]Vipin Kumar, [1]Léna Cauchie, [1]Anne-Sophie Mreyen, [2]Mihai Micu, [1]Hans-Balder Havenith

[1]Georisk and Environment, Department of Geology, University of Liege, Belgium
[2]Institute of Geography, Romanian Academy, Bucharest, Romania

Correspondence: Vipin Kumar (v.chauhan777@gmail.com)

Abstract

There have been many studies exploring the rainfall induced slope failures in the earthquake affected terrain. However, studies evaluating the potential effects of both landslide triggering factors; rainfall and earthquake have been infrequent despite the rising global landslide mortality risk. The SE Carpathians, which have been subjected to many large historical earthquakes and changing climate and thus resulting in frequent landslides, is one such region that is least explored in this context. Therefore, a massive (~9.1 Mm²) landslide, situated along the Basca Rozilei River, in the Vrancea Seismic Zone, SE Carpathians is chosen as a case study area to achieve the aforesaid objective using slope stability evaluation and runout simulation. The present state of slope reveals the Factor of Safety in a range of 1.17-1.32 with a static condition displacement of 0.4-4 m that reaches up to 8-60 m under dynamic (earthquake) condition. The Groundwater (GW) effect further decreases the Factor of Safety and increases the displacement. Ground motion amplification enhances the possibility of slope surface deformation and displacements. The debris flow prediction, implying the excessive rainfall effect, reveals a flow having 9.0-26.0 m height and 2.1-3.0 m/sec velocity along the river channel. The predicted extent of potential debris flow is found to follow the trails possibly created by previous debris flow and/or slide events.

Key words: Landslide; Earthquake; Rainfall; Slope Stability; Runout; SE Carpathians.

1 Introduction

Landslides, though a normal process of hillslope erosion, pose socio-economic risk to human life and infrastructure (Gupta et al. 2017; Froude and Petley 2018; Pollock and Wartman 2020; Kumar et al. 2021). Despite the rising global landslide mortality risk, effective evaluation of disastrous influences of landslides has been infrequent (Sassa 2015; Haque et al. 2019; Klimes et al. 2019). Such evaluation approaches could be regional (susceptibility/hazard/risk/vulnerability) or local (slope stability, runout prediction, monitoring/change-detection mapping) (Fell and Hartford 1997; Westen et al. 2006; Margottini et al. 2013; Hungr 2018). However, effectiveness in such approaches cannot be justified until the main landslide triggering factors; rainfall and earthquake are evaluated together. Despite the numerous case studies of rainfall induced slope failures in the earthquake affected terrain (Lin et al. 2006; Helmstetter et al. 2010; Tang et al. 2011; Durand et al. 2018; Bontemps et al. 2020), studies predicting the potential effects of both factors have been relatively rare. Necessity of such studies becomes more critical in view of an annual average of >4000 landslide related deaths worldwide in the last decade (Pollock and Wartman 2020).

Owing to the capability to represent the progressive deformation in the slope under various loading conditions, numerical modeling based analysis can be considered as one of the few approaches for effective evaluation of slope instability and associated risk (Jing 2003; Fenton and Griffiths 2008). Though the continuum modelling based approaches have been common for local scale evaluation of hillslope response (Griffiths and Lane 1999; Jamir et al. 2017; Kumar et al. 2018; 2021), their limitations in estimating large strain, particularly during the dynamic analysis makes the discontinuum modeling better option (Havenith et al.2003; Bhasin and Kaynia 2004). Apart from the stability evaluation, prediction of potential run-out during the slope failure constitutes a principal risk evaluation approach (Hungr et al. 1984; Hutter et al. 1994; Rickenmann and Scheidl 2013). Among different types of landslides, debris flows have shown the maximum outreach, relatively more fatality, and secondary effects like river damming and subsequent outburst flood (Jakob et al. 2005; Ding et al. 2020; Kumar et al. 2021). Among different run-out prediction approaches, dynamic model based Rapid Mass Movement Simulation (RAMMS) (Christen et al. 2010), Flo-2D (O’Brien et al. 1993), and MassMov2D (Beguer´ıa et al. 2009) have been relatively more useful (Rickenmann and Scheidl, 2013; Kumar et al. 2021).

In view of these understandings, the present study aimed to infer the potential response of a landslide slope under the seismic and extreme rainfall conditions using stability evaluation and runout simulation. Such simulations/modeling outputs depend upon certain input parameters and criteria, the values of which might be affected by uncertainties due to nonlinear behavior of material. Therefore, a parametric analysis is also performed to evaluate the uncertainty. In order to achieve the aforementioned objectives, a massive (~9.1 Mm²) landslide in the Vrancea Seismic Zone, SE Carpathians is chosen as a case study area. The region has been subjected to frequent earthquakes and relatively wet climatic conditions that induce frequent landslides and related socio-economic losses (Micu et al. 2013; 2016; Micu, 2019; Mreyen et al. 2021).

2 Study area

2.1 Geological setting & geomorphology

The landslide is situated at latitude 45° 30' 23" N, longitude 26° 25' 05" E along the Basca Rozilei River in the SE Carpathians, Romania (Fig. 1). The earliest record of this landslide is mentioned in the geological map by Murgeanu et al. (1965). Unfortunately, no previous record and/or dating are available at present. The slope is composed of shale belonging to the Miocene thrust belt that separates the external foredeep in the north, east, and south-east from the inner Carpathians mountain ranges. Thrust faults, strike-slip faults, and folds traverse the region in and around the vicinity of landslide slope. The origin of these structural features has been related to the Eocene-Miocene collision of Alcapa and Tisza-Dacia plates against the Bohemian and Moesian promontories that gave rise to the Carpathians Mountain (Tischler et al. 2008). The SE part of the Carpathians, however, is still uplifting at a rate of 3-8 mm/yr. due to the foreland coupling of the converging plates (Pospisil and Hipmanova 2012; Mațenco 2017).

The landslide toe along the river hosts the 'Varlaam' village (Fig. 1, 2a). The landslide has a slope gradient ranging between 15°-20° and encompasses an area of ~9.1 Mm². The landslide-affected area is covered by shrubs and scattered trees towards its flanks and with grasslands in the inner parts, mainly used as pastures and hayfields. The landslide crown region has a depression that might be a surficial imprint of the paleo-detachment (or depletion zone) (Fig. 2b). Near the right (or southern) flank, a seasonal flow channel (or gully) emerges near the paleo-detachment depression and finally merges at the river channel (Fig. 2c). Near the left (or northern) flank, slope surface comprises flow relics, possibly of paleo-debris flow and/or slide events (Fig. 2d), as also inferred from loose/unconsolidated deposit at the slope toe (Fig. 2e). This flow deposit is noted to develop 100-150 m wide minor scarps (Fig. 2e). Such scarps may further grow and result in the debris flows during extreme rainfall and/or earthquake events and hence pose a risk to the nearby human settlement.

2.2 Rainfall and earthquake regime

The study area is subjected to an increasing rainfall trend (Fig. 3a). The average monthly rainfall has been 50 ± 1.6 (SE) mm during the years 1982-2019 that has increased in recent decades (2000-2019) to 53 ± 2.3 (SE) mm (Fig. 3b). Monthly rainfall patterns further reveal relatively higher rainfall in the months of May, June, and July (Fig. 3c). Such enhanced summer (June-July) rainfall has been related to the existing positive phase of the North Atlantic Oscillation (NAO) index that allows the strengthening of continental climate, Mediterranean retrogressive cyclones, and Siberian High in central and southern Europe (Constantin et al. 2007; Magyari et al. 2013; Obreht et al. 2016).

Apart from the rainfall, soil moisture and surface runoff also show increasing trend during the years 1982-2019 (Fig. 3d, g). Though the average monthly soil moisture and surface runoff also increased in recent decades, their trends do not follow rainfall entirely (Fig.3e, h). It occurs due to the fact that the temporal coexistence of rainfall, surface runoff, and soil moisture depend upon rainfall threshold and soil conditions (antecedent soil moisture). Further, the surface runoff (water, from precipitation that flows over the land surface) correlates relatively well with the rainfall unlike the soil moisture that retains part of the rainfall before achieving saturation and hence do not correlate well (Supplementary Fig. 1). This difference of correlation is further visible in the monthly pattern (Fig. 3f, i). It is to note that the surface runoff and soil moisture data are based on the FLDAS (Famine Early Warning Systems Network Land Data Assimilation System) model (McNally et al. 2018). It utilizes precipitation datasets & analyses like CHIRPS (Climate Hazards Group InfraRed Precipitation with Station data) & MERRA2 (Modern-Era Retrospective analysis for Research and Applications, Version 2) along with land cover data to derive variables like soil moisture and surface runoff.

Further, the daily rainfall data of the years 2000-2019 revealed 48 extreme rainfall events (Fig. 3j). ‘Extreme’ rainfall pertains to >30 mm/24h in the region on the basis of previous studies exploring the rainfall variability (Apostol 2008; Croitoru et al. 2016). Out of these 48 events, 28 events occurred in the last decade, particularly in the years 2005, 2007, 2010, and 2016. The debris flows and flash floods in the region in the years 2005 and 2010 (Micu et al. 2013; Grecu et al. 2017) can be related to these extreme rainfall events in the region. The year 2005 and 2010 had relatively high precipitation due to synoptic conditions that involved pressure lows and front systems moving along a SE–NW trajectory from the Mediterranean Sea and Black Sea towards Central Europe and in west to east direction from the Atlantic Ocean to Eastern Europe. These trajectories led to severe flood and slope failure events in different parts of the Central and Eastern Europe (Mihailovici et al. 2006; Micu et al. 2013; Grecu et al. 2017). The influence of these trajectories is also visible in the regional rainfall pattern (Supplementary Fig. 2), where year 2005 and 2010 have relatively higher rainfalls. Though the years 2007 and 2016 also had many extreme rainfall events, these years didn't have as high surface runoff as year 2005 and 2010 (Fig. 3h). Notably, many conceptual and physically based models have been proposed relating the initiation of debris flow to surface runoff conditions (Simoni et al. 2020).

Further, the temporal pattern of relatively higher values (above-average) of rainfall, surface runoff, and soil moisture revealed that May-September months dominate the trend having majority of the events when all three variables had extremes (i.e., above-average) (Fig. 3k). These 'above-average' values refer to the monthly scale. The temporal overlapping of these variables further justifies the occurrence of debris flows and flash floods in this region in the last decade and possibility of more such events in the near future (Micu et al. 2013; Ilinca 2014; Grecu et al. 2017; Micu et al. 2019).

Apart from the temporally enhanced rainfall, surface runoff, soil moisture, the study area is also subjected to frequent earthquakes owing to its position in the Vrancea Seismic Zone that is one of the most active seismic zones in Europe (Fig. 4a, b). This region has received ~469 earthquakes ($M_w \geq 4$) during the years 1960-2019. The earthquake event cluster represents a NE-SW trend (Fig. 4b). About 75 % of the total earthquake events occurred in a depth range of 60-180 km (sub-crustal depth) and 4 out of 5 events having a magnitude ≥ 6 occurred within 60- 100 km depth (Fig. 4c). The relative dominance of M≥ 6 earthquakes in this depth range has been related to the reverse faulting mechanism in this depth range (Radulian et al. 2007; Petrescu et al. 2019). The possible explanation of the pattern of earthquakes has been divided in the following two categories; (1) it might be associated with descending relic ocean lithospheric beneath the bending zone of the SE Carpathians , or (2) it might be associated to continental lithosphere that has been delaminated, after the collision (Bokelmann and Rodler, 2014; Petrescu et al. 2019).

Though the majority of earthquakes have their magnitude smaller than 5 and quite deep (mostly between 60 and 180 km), their epicentres are situated within 50 km from the study area (Fig. 4d). Such intermediate to deep earthquakes in Vrancea region (study area) have triggered landslides as far as 250–300 km from their epicentres (Havenith et al. 2016). Further, any major future earthquake might have ground effects in a much larger area (150000 km^2), possibly causing more landslides (Havenith et al. 2016). Regional distribution of the annual rainfall and earthquakes around the study area is also shown in Supplementary Fig. 3.

3 Methodology

In order to evaluate the landslide response under seismic and extreme rainfall conditions, our approach involved dynamic slope stability analysis and runout simulation, respectively. Both the techniques required a landslide model that was constructed using field based ambient noise analysis, empirical equations/values, digital elevation model, and geological modelling software. Details are as follows;

3.1 Debris (or loose material) depth estimation

We analysed seismic ambient noise at 56 measure points to estimate the depth of impedance contrasts. The equipment was composed of 7 velocimeters Güralp CMG-6TD 30s and 1 velocimeter Lennartz 5s and Cityshark II. The technique aims at estimating the site resonance frequency by computing the spectral ratio between horizontal (NS, EW) and vertical components (Nakamura, 1989). Under particular geological conditions where impedance contrast exists at depth, as representative of a loose/soft material overlying bedrock, the resulting Horizontal to vertical spectral ratio (HVSR) curve presents a peak in correspondence of the site resonance frequency (f_o). Fig. 5a represents the location of the inferred f_o in a range of <1.5-4.5 Hz. Lower frequencies, generally implying relatively higher thickness of loose material, are noted in the central part and near the right flank.

The thickness (h) of the loose/soft material is consecutively estimated using the shear-wave velocity (V_s) and resonance frequency (f_o) using the following equation (Murphy et al. 1971; Ibs-von Seht & Wohlenberg 1999);

$$\mathbf{h=V_s/\,(4*f_o)} \qquad \textbf{Eq. 1}$$

In view of the similar litho-tectonic conditions and spatial proximity, the shear-wave velocity (V_s) values in the present study are based on Mreyen et al. (2021). For the loose overburden (soil) and rockmass, the V_s are taken as ~400 m/sec and ~900 m/sec, respectively.

The thickness of the loose material (inferred from the HVSR and V_s) at different measurement locations was later imported in the LeapfrogGeo software (v. 5.1) along with the surface morphology (Fig. 5b). The surface morphology with a spatial resolution of ~12 m is based on the TanDEM-X (TerraSAR-X add-on for Digital Elevation Measurement) digital elevation model. The surface morphology and depth information of loose material were integrated using the LeapfrogGeo (v.5) to construct a continuous soil thickness layer and hence a 3D model of the landslide (Fig. 5c, d). This model was later used to extract the 2D slope sections (CS-1, CS-2, CS-3, and CS-4) for the slope stability evaluation (sec. 3.2) and runout simulation (sec. 3.3).

3.2 Slope Stability evaluation

The 2D slope sections (CS-1, CS-2, CS-3, and CS-4), shown in Fig. 6a, were used to determine the hillslope response under static (gravity) and dynamic (seismic) conditions by performing the slope stability analysis in the UDEC v.6 (2014) software. Each slope section comprises loose overburden (soil) over rockmass and an interface joint separating these blocks (Fig. 6b-e).

Under static condition, factor of safety of slope and potential material displacement are determined, whereas under dynamic condition, potential material displacement, Peak Ground Acceleration (PGA), and spectral ratio are evaluated. The factor of safety is determined using Shear Strength Reduction approach (Matsui and San 1992; Griffiths and Lane 1999). The potential material displacement under static condition refers to displacements after the model has reached static equilibrium under gravity load. The spectral ratios are used to understand the response of the medium to the input signal by comparing the signals obtained in the monitoring points at the surface with the signal at the monitoring point at depth (base) (McCowan and Lacoss 1978).

For the PGA and spectral ratio, material models are considered as elastic, whereas for the factor of safety and material displacement (static/dynamic) calculations, elasto-plastic models are considered. Elastic material model involved modulus (elastic/shear/bulk) values of the rock mass and soil. In elasto-plastic conditions, Modified Hoek-Brown (MHB) plasticity criteria (Hoek et al. 2002) and Mohr-Coulomb (M-C) plasticity criteria (Coulomb 1776; Mohr 1914) are used for the rock mass and soil, respectively. The joint plane is assigned Coulomb-Slip criteria (Coulomb 1776) in both elastic and plastic conditions. For dynamic analysis, two different signals, i.e. Ricker wavelet (Ricker 1943) and a signal record of the 1976 Friuli Earthquake, are used (Fig. 8).

The Ricker wavelet, a theoretical waveform, provides an advantage to be a relatively short signal marked by an energy distributed over a range of frequencies. Therefore, the PGA and spectral ratios are evaluated using the Ricker wavelet to understand the ground motion amplification on the landslide surface. Notably, in many studies such ground motion amplification is found to enhance the slope instability (Lenti and Martino 2012; Gaudio et al. 2014). The Ricker wavelet has been used in several studies owing to its reliable representation of seismic waves propagating through the viscoelastic homogeneous media (Bourdeau et al. 2004; Gholamy and Kreinovich 2014). Further, the displacement is determined using both dynamic signals (Ricker wavelet and Friuli earthquake, 1976) to evaluate the difference.

Soil and rock mass blocks in the cross sections (CS-1 to CS-4) were discretized into finite difference zones of 6m and 20m size, respectively according to the following relation (Kuhlemeyer and Lysmer, 1973);

$$\Delta l \leq \lambda/10 \text{ or } \leq \lambda/8 \qquad \textbf{Eq. 2}$$

Here, Δl = zone size, λ = wavelength associated with the dominant frequency. 'λ' can be determined using λ= C/f, where C is the speed of wave propagation associated with the fundamental frequency (f). For the 'C' (or shear wave velocity) of soil and rock mass, we used 400 m/sec and 900 m/sec, respectively (sec. 3.1). The 'f'=2.0-4.5 Hz was considered as a central frequency range. The lateral boundaries in all four slope sections (or models) were considered as free-field owing to near surface position of hillslope (Fig. 6). A stress-boundary condition (Joyner and Chen 1975; UDEC v.6, 2014) was applied at the base in which horizontal direction is considered as viscous, whereas vertical direction is kept free. This stress-boundary condition converts seismic input from velocity wave to stress wave. To approximate the natural attenuation in the models during the seismic loading, Rayleigh damping with a 0.02 damping ratio (i.e., 2% fraction of critical damping and 2.5 Hz central frequency was used with the both mass and stiffness damping. Though most of the soil types and rock mass possess the damping in the 2%-5% fraction of the critical damping (Biggs

1964), plasticity models (M-C criteria) and presence of joints result in further energy loss (UDEC v.6 2014). Therefore, the damping ratio was kept at the lower level of the suggested range.

Since, the area is subjected to temporally enhanced rainfall (sec. 2.2) and some studies have noted the percolation of rainfall water in the loose material resulting in the Groundwater (GW) level increase and subsequent slope instability (Van Asch et al. 1999; Liang 2020), effect of the GW is also explored. To simulate the GW effect, coupled hydraulic (fluid flow)-mechanical analysis was used in which mechanical deformation and joint fluid pressure affect each other as analysis progresses. Further, model was brought to static equilibrium before performing Factor of Safety (FS) calculations. Notably, FS calculations were also performed under mechanical stress only (without GW). Steady-state (water table) fluid flow analysis was used to simulate fluid flow. The GW is included in static as well as in dynamic analysis in plasticity conditions. The UDEC allows the GW simulation through the joints as per the parallel plate model (Witherspoon et al. 1980). The parameters and their values used in the static and dynamic analysis are mentioned in Table 1.

A parametric analysis was also performed to justify the selection of values of different input parameters by evaluating the change in the output parameters in response to the change in different input parameters. Out of four slope sections, the CS-2 and CS-3 were chosen to perform the parametric analysis in view of their central position in the landslide and the heterogeneity in soil thickness and topography (Fig. 6c, d). In order to understand the effect of the GW level change, two GW levels were considered in the CS-2 and CS-3 sections. Since the UDEC simulates the fluid flow through joint aperture, the GW level change is manifested by different heights (h1, h2) of the GW at the joint. Here, the difference of h1 and h2 i.e., Δh is 10m (Fig. 6d). Among the different input parameters listed in Table 1, angle of internal friction of soil, joint friction angle, groundwater head, and elastic modulus were used for the parametric analysis. It is to note that the bulk and shear modulus were also changed along with elastic modulus because all three modulus parameters are interrelated (Mc Dowell 1990). Though each parameter might have a certain effect on the output, these four have been noted to affect the Factor of Safety and displacement relatively more (Kumar et al. 2021).

3.3 Run-out simulation

The hillslopes affected by the seismic shaking have also been noted to be more prone to rainfall induced slope failures, particularly in the form of debris flows (Shieh et al. 2009; Tang et al. 2011). Such debris flows can initiate either by increased pore pressure or runoff involving entrainment (Godt and Coe 2007). Thus, the increased frequencies of the extreme rainfall, soil moisture, surface runoff, and recent debris flows events in the region (sec. 2.2), escalate the possibility of debris flow in the Varlaam landslide.

To ascertain the outreach of such potential debris flow during an extreme rainfall event, Voellmy-Salm (Voellmy 1955; Salm 1993) fluid-flow continuum model based Rapid Mass Movement Simulation (RAMMS) software was used. The RAMMS divides the frictional resistance into a dry-Coulomb type friction (μ) and viscous-turbulent friction (ξ) (Christen et al. 2010). The frictional resistance S (Pa) is thus;

$$\boldsymbol{S=\mu N + (\rho g u^2)/\xi} \qquad \textbf{Eq. 3}$$

Where $N= \rho hg\cos(\psi)$ is the normal stress on the running surface, ρ= density, g= gravitational acceleration, ψ = slope angle, h= flow height and u= (u_x, u_y), consisting of the flow velocity in the x- and y-directions. A detailed description of the governing equations is presented in Supplementary data.

Generally, the values for μ and ξ parameters are achieved using the reconstruction of real events through simulation and subsequent comparison between dimensional characteristics of real and simulated event. However, the toe of Varlaam landslide merges with the river floor and hence there is an uncertainty in reconstruction of the volume of previous flow events that has been washed away by the river. Therefore, μ and ξ are taken in view of topography of landslide slope and run-out path, landslide material, and based on previous studies/models (H¨urlimann et al. 2008; Rickenmann and Scheidl 2013; RAMMS v.1.7.0). In this study, maximum allowable friction (μ) i.e., μ= 0.4 (or ϕ = 21.8°) was used with the turbulence (ξ) of 250 m/sec² (Table 2). Different depths were considered as block release in view of uncertainties to ascertain the exact depth of loose material that will be eroded/entrained during the debris flow. Though the landslide surface has some relics of flow channels near left flank (Fig. 2d, e), the data pertaining to the spatial-temporal pattern of discharge at these flow channel/gullies was not available. Therefore, the release area is chosen as block release because it has been more appropriate when the flow path (e.g. gully) and its possible discharge on the slope is uncertain (RAMMS v.1.7.0). The runout stopping criterion is based on momentum threshold, which was considered as 5 % of moving mass. A sensitivity analysis is also performed to evaluate the possible influence of frictional parameters on the debris flow characteristics. Further, in order to understand the influence of river channel morphology on the debris flow characteristics, their inter-relationship is also sought.

4 RESULTS & DISCUSSION

4.1 Slope stability evaluation

4.1.1 Factor of Safety (FS) & displacement

The FS of slope varies in a range of 1.17-1.32 that decreases further to 1.09-1.29 under Groundwater (GW) condition (Fig. 8). In both cases, the CS-2 model attains lowest FS implying relatively more instability. The displacement in loose material was obtained in static, static with fluid (GW), dynamic, and dynamic with fluid (GW) conditions. Under the static condition, displacement ranges between 0.4-4.0 m that increases to 0.68 m-18 m under the GW condition with minimum at CS-1 and maximum at CS-2 (Fig. 8). Under dynamic condition, displacement ranges from 8-60 m, and further increases to 7.5-62 m by combining dynamic with GW conditions. Similar to the static condition, minimum displacement is noted at CS-1, whereas maximum at CS-2. Further, in all sections (CS-1 to CS-4), displacement accumulated mostly at the upper part of the debris layer (i.e., landslide crown) or at the steepest portion of slope surface. This spatial affinity of displacement and steep gradient is caused by the influence of topography on the material displacement (Kumar et al. 2021). Notably, this dynamic displacement pattern pertains to the Friuli earthquake signal (Fig. 7c,d). A comparison of the static and dynamic displacement (caused by the Friuli earthquake signal and Ricker wavelet) is presented in Fig. 9.

As also shown in Fig. 9, the GW condition enhanced the displacement in static as well as in dynamic conditions (Fig. 9). Static displacement showed least scattering as evident from the median level and least difference of Max. and Min. values. Further, except for the CS-2 section, all three sections (CS-1, 3, 4) have relatively low dynamic displacement in dry and wet (GW) conditions due to the Ricker wavelet than compared to the displacement caused by the Friuli signal (Fig. 9a-d). This difference may be attributed to the response of steep topography (of CS2 model) to the high energy Ricker wavelet signal (Fig. 7b).

Thus, it can be understood that 'Varlaam' hillslope, situated in the region having frequent extreme rainfalls and earthquakes, attains more instability under saturated-dynamic conditions.

4.1.2 Parametric analysis

The Factor of Safety (FS) of slope increased in response to increase in angle of internal friction of soil, joint friction, and elastic modulus (Fig. 10). Such increase in the FS (~7% in the CS 2) is attained by increasing the angle of internal friction of soil. This effect is attributed to the 'Shear Strength Reduction (SSR)' approach. The GW level increase resulted in a decreasing FS because the increased GW level increased the joint flow rate and thus enhanced the fluid pressure on the overlying medium i.e., soil. This increased fluid pressure further decreased the normal stress and hence the shear stress of the overlying soil, as per Mohr's Criteria (Mohr 1914). Such decrease in the shear stress of soil resulted in the decreased FS.

Owing to their spatially variable nature, static and dynamic displacements are represented in a range of maximum (max.) and minimum (min.) in Fig. 10. Static displacement decreased on increasing the angle of internal friction of soil, joint friction, and elastic modulus. Such decrease (~40% in CS 2 and ~38 % in CS3) occurred in response to the modulus increase. This decrease in the displacement refers to fact that increased modulus increases the normal and shear strength of the soil and hence displacement will decrease on increasing the modulus (Hara et al. 1974). The GW level increase resulted in the increased static displacement (~16% in CS2, ~36% in CS3). Such increase in the static displacement is attributed to the decreased shear strength of soil due to the increased joint fluid pressure (Witherspoon et al. 1980). Similar to the static displacement, dynamic displacement decreased on increasing the angle of internal friction of soil, joint friction, and elastic modulus and increased on increasing the GW level. Along with the modulus, angle of internal friction of soil is also noted to decrease (~16% in the CS2, ~21% in the CS 3) the dynamic displacement relatively more. The increase in the GW level resulted in 8% and 33% increase in the CS2 and CS3 models in dynamic displacement.

Notably, present study utilized approximated values of the input parameters for the slope stability analysis (Table 1). Though the approximated values cannot replace the values measured in the geotechnical analysis, parametric analysis minimizes the uncertainty caused by selection of specific values by exploring the possible output pattern.

Thus, by utilizing the central values (highlighted as grey in Fig. 10) in the slope stability analysis (sec. 4.1.1), present study attempted to minimize such uncertainty in the findings. Further, though the GW was also used in the UDEC models to infer the influence of saturation on slope stability, potential response of the slope under excessive saturation (extreme rainfall) is further explored using the debris flow runout simulation (sec. 4.2).

4.1.3 Peak Ground Acceleration (PGA)

Apart from the FS and displacement, ground motion (acceleration) amplification was also evaluated to understand the potential seismic deformation at the slope surface (Fig. 11). The input seismic signal for the following acceleration pattern is presented in Fig. 7a. For all four models (CS1 to CS4), the PGA values at the river floor (RF) ranges between 5.78-7.47 m/sec^2 (0.58g – 0.74g), whereas at the rock mass surface above the landslide crown (CR) it varies from 6.37 to 10.19 m/sec^2 (0.65g -1.03g) (Fig. 11). At the model base (MB), maximum acceleration remains between 3.79-3.90 m/sec^2 (0.38g -0.39g).

Thus, the PGA at the river floor (RF) amplifies~1.5-2.0 times from the maximum acceleration at the model base, whereas at the rock mass surface above the landslide crown, it amplifies ~1.7-2.7 times from the maximum acceleration at the model base. Such amplification of the PGA at the rock mass surface above the landslide crown can be attributed to the topographic irregularity and upward propagation of seismic waves where they meet preceded waves produced on the relatively horizontal surface of the slope (Jibson 1987; Havenith et al. 2003; Bourdeau and Havenith 2008; Luo et al. 2020).

The debris surface, however, attains relatively higher PGA in all four models than the rock mass surface as noted at the following three monitoring stations; DB_Lw, DB_Md, and DB_Up (Fig. 11). At the lower part of the debris (DB_Lw), the PGA ranges from 8.3 to 12.13 m/sec^2 (0.84g-1.23g) that further grew at the middle part of the debris (DB_Md) and attaines10.17-14.40 m/sec^2 (1.03g-1.46g). The maximum PGA is attained by the upper part of the debris (DB_Up) with a range of 7.26-18.50 m/sec^2 (0.74g - 1.88g). Such relatively high PGA at the debris surface can be referred to the impedance contrast between underlying rock mass and overlying soil and/or partial loss of the shear strength during seismicity (Novak and Yan, 1990; Safak, 2001).

Detailed evaluation at different monitoring points in each model are as follows; Model Base (MB) and River floor (RF) monitoring points have almost similar maximum acceleration values in all four models. At the lower part of the debris i.e., DB_Lw, relatively higher PGA is attained by the CS3 model (~12.1 m/sec²) followed by the CS2 model (~10.8 m/sec²) in comparison to DB_Low points of CS1 and CS4. Relatively higher PGA is attributed to lower soil thickness below this monitoring point in the CS3 and CS2 models that could be the main reason for acceleration amplification as also stated by Murphy et al. (1971); Beresnev and Wen (1996).

At the middle part of the debris i.e., DB_Md, relatively higher PGA is attained by the CS2 model (~14.4 m/sec²). Notably, despite the relatively higher soil thickness, this monitoring point obtained a relatively higher PGA. It possibly occurred due to irregular topography of the CS2 model that generally results in interference of direct and scattered waves and hence amplification of ground motions (Asimaki and Mohammadi 2018).

At the upper part of the debris i.e., DB_Up, relatively higher PGA is attained by the CS1 model (18.5 m/sec²) followed by the CS4 model (15.8 m/sc²). The effect of soil thickness below this monitoring point, as explained for the lower part of debris, could be the main reason for such amplification at this monitoring point in these models. Monitoring point at rock mass surface above the landslide crown (CR) too has almost similar PGAs in all the models except the CS3 model. Relatively higher PGA (10.19 m/sec²) at the CR monitoring point of CS3 model might be due to its position on steeper surface, whereas CR points at other models are at relatively flat surface.

4.1.4 Spectral Ratio

The ground motion amplifications were also explored using the spectral ratios at two central slope sections; CS-2 and CS-3 (Fig. 12). In both models, the (River Floor) RF point showed no significant amplification at any particular frequency, possibly due to the flat surface positioning. In CS2 model, Debris Lower part (DB_Lw) point shows notable amplification at 2.0-2.5 Hz with minor amplification at 4.5-5.0 Hz, whereas in the CS 3 model, DB_Lw point shows attenuation (or de-amplification) near ~2 Hz and slight amplification at 4.5-6.0 Hz. The contrast of amplification and de-amplification at ~2 Hz is attributed to the geometrical variation in topography because the DB_Lw point in the CS2 is situated at a relatively elevated surface, whereas in the CS3, at a relatively shallow surface. Minor geometrical variations at the slope toe have been observed to result in de-amplification at low frequencies in other studies also (Bouckovalas and Papadimitriou, 2005).

Notably, along with the DB_Lw point, Debris Middle part (DB_Md) and Debris Upper part (DB_Up) points in both the models also have minor/major amplification at 4.5-6.0 Hz. This coexistence of amplification at a certain frequency range by different monitoring points at debris surface may be attributed to impedance contrast between debris and underlying rock mass. Further, the DB_Md point in both the models showed amplification at ~1.0 Hz and 2.0-2.5 Hz. The amplification at lower frequency i.e.,~1.0 Hz may be attributed to the thick (40-60m) layer of debris that possibly decreases the resonance frequency and results in amplification of ground motion as also reported by Beresnev and Wen (1996). The amplification at 2.0-2.5 Hz may be referred to the elevated topography at these points in both the models.

The DB_Up point in both the models has different responses. In the CS2 model, it showed amplification at 1.0-1.5 Hz, whereas in the CS3 model, spectral ratio is relatively stagnant except minor amplification at 4.0 & 6.0 Hz. This contrast may be understood by the fact that in the CS2, this monitoring point is situated at a thicker and elevated surface, whereas in the CS3, it is situated at relatively shallow topography and on top of relatively thin landslide thickness. Finally, the Crown (CR) point also has a different spectral ratio in both the models. It shows higher amplification in the CS3 model than the CS2 model that may be referred to the positioning of these points. The CR in the CS2 is situated at a relatively flat surface unlike in the CS3 model where it is situated at a steep surface. Thus, the monitoring points showed amplification at multiple frequency range that is attributed to complex topography of landslide, soil thickness variation, and impedance contrast.

4.2 Landslide runout pattern

In view of uncertainties to ascertain the exact depth of loose material that will be eroded/entrained during the debris flow, runout pattern was evaluated at four different release area depths; 5m, 10m, 15m, and 20m of the loose overburden (Fig. 13a, b). The identification of release area was based field and satellite imagery observations. Following four factors; gullies (Fig. 2c), flow relics (Fig. 2d), signs of failure (Fig. 2e), and overburden thickness pattern (Fig. 5c) were considered while selecting the release area. The thickness region of 60-80 m having flow relics and signs of failure were therefore selected as the potential release area (Fig. 13b). Debris flow characteristics (flow height/flow velocity) of the debris flow that will strike the river floor during such an event are also inferred along the river channel (Fig.

13c). Debris flow height and velocity at hillslope and along the river channel are summarized in Table 3.

As can be seen from Fig. 13, increasing depth of the release area increases the flow characteristics at hillslope. However, the flow characteristics vary once strike the river floor. Debris flow height increases towards downstream part of the river channel on increasing the depth of material (Fig. 13f, i, l, o). This behaviour can be referred to the gully/channel on the hillslope near the downstream part (Fig. 2c) that possibly accelerated the flow. Debris flow velocity, however, decreases on increasing the depth of material. Relatively higher flow velocity at lower material depth (Fig. 13f) can be understood using “turbulence (or Chezy resistance): ξ” factor used in the Eq. 3. The Chezy resistance is famous as "turbulent" friction (Voellmy, 1955) since the mathematical formulations are similar to the well-known turbulent Chezy equation (Chow 1959). According to ‘Chezy’ equation, lower material thickness results in higher flow velocity. Further, apart from such turbulence effects, river channel morphology also affects the flow characteristics. As can be seen in Fig. 14a-c, lower channel width (narrow sections) generally accommodates higher flow velocity and height, of course with some non-linearity as seen at 10 m depth (Fig. 14a). Further, increasing the material depth increase the flow height relatively more than flow velocity (Fig. 14c).

By keeping the maximum friction (μ=0.4) as constant, sensitivity analysis was also performed by using different turbulence coefficients (Fig. 14d-f). It revealed that flow height and velocity increase on increasing the turbulence coefficient (implying increasing liquid content). It is to note that the central value i.e., 250 m/sec^2, showing the moderate response, is used in the main findings, as also mentioned in Table 2. Further, flow velocity is found more responsive at lower turbulence, whereas at higher turbulence, flow height dominates (Fig. 14f). Further, in order to understand the extent of runout along the river channel, runout results at maximum release area depth were also laid over the Google Earth imagery (Fig 15a, b). A top view of the landslide with the runout is shown in inset ‘c’. The predicted runout is noted to extend across the river channel mainly at two locations, one near the left flank (Fig. 15d) and the other near the right flank (Fig. 15e). At both of these locations, the river channel attains sinuosity in a range of ~1.30-1.32 (shown through channel length measurement). River channel might owe this sinuosity to the paleo-landslide and/or fluvial deposit that is extending the slope toe at these locations. Thus, the runout findings of present study are noted to follow the same spatial extent as possibly followed by previous landslide events.

5 SUMMARY

The present state of slope reveals an instability condition through the Factor of Safety in a range of 1.09-1.32 and potential displacement near the landslide crown (Fig. 8, 9). Such a displacement near the landslide crown may be related to the development of shear failure in slopes (Matsui and San, 1992; Kumar et al. 2018; 2021). The possibility of shear failure becomes more viable in case of degradation of shear strength of slope material and/or rupture planes. Notably, both the main landslide triggering factors; rainfall and earthquake have been found to degrade the shear strength of slope material through the percolation and shaking induced particle movements, respectively (Cai and Ugai, 2004; Chang and Taboada 2009). The GW, implying the rainfall induced percolation effect, decreases the Factor of Safety and increases the material displacement. This effect is attributed to the joint hydraulic pressure against the overlying loose material that decreases the normal stress and hence the shear strength of overlying loose material (Mohr, 1914; Witherspoon et al. 1980). Similar to the GW effect in static condition, the combined response of the dynamic force and the GW resulted in an increase of the displacement (Fig. 8). It can be attributed to the fact that seismic shaking increases the hydraulic pressure in the joints that causes enhanced material displacement in the overlying loose material (Wang et al. 2010).

Further, the ground motion amplification also revealed the slope instability (or potential deformation). The maximum value of Peak Ground Acceleration (PGA) is attained by the upper part of the debris surface (near the landslide crown) (Fig. 11). It is referred to the impedance contrast between underlying rock mass and overlying soil and/or partial loss of the shear strength during seismicity (Novak and Yan, 1990; Safak, 2001). Further, the spectral ratio also showed signal amplification, at multiple frequency range, at the debris surface (Fig. 12). Such an amplification at multiple frequency ranges is attributed to complex topography of landslide, soil thickness variation, and impedance contrast (sec. 4.1.4). Such high amplification at the slope surface has been considered as a main cause of slope failure in many other studies also (Lenti and Martino, 2012; Gaudio et al. 2014).

As also stated in sec. 3.3, hillslopes affected by the seismic shaking have also been prone to rainfall induced failures, particularly in the form of debris flows. Further, the earthquake induced shear strength degradation of slope material may also result in the enhanced entrainment during a debris flow event (Liu et al. 2020). These debris flows might be initiated either by increased pore pressure (or GW induced hydraulic pressure) or runoff involving entrainment (Godt and Coe 2007). Though the GW effect is obtained on the slope instability (Fig. 8, 9), potential response of the slope under excessive rainfall is explored through debris flow runout analysis (Fig. 13, 14, 15).

The debris flow runout predictions revealed a non-linear increase in the debris flow height and velocity along the river channel on increasing the depth of release area (Fig. 13). This non-linearity is attributed to the variation in the river channel width (Fig. 14) and influx of debris flow material from the slope. Though the present study noted the influence of channel morphology on the debris flow characteristics, other studies have observed the changes in channel morphology caused by the debris flows (Remaître et al., 2005; Simoni et al. 2020).

Thus, there seems to be a positive feedback process between channel morphology and debris flow that is further strengthened by the finding of debris flow extent across the river channel (Fig. 15d, e). At both of these locations, slope toe extends towards the E-SE direction resulting in higher channel sinuosity. These extended slope toes probably represent paleo-landslide and/or fluvial deposits. Signs of flow relics at the slope surface & failure at slope toe at these locations (Fig. 2d,e) further support the possibility of paleo-landslide deposit. Thus, the predicted extent of potential debris flow is found to follow the trails possibly created by previous landslide flow and/or slide events. Aforementioned findings, temporally increasing rainfall, soil moisture, and surface runoff (sec. 2.2), and frequent debris flows/flash floods in this region (Micu et al. 2013; Grecu et al. 2017; Micu et al. 2019) pose increasing risk of debris flow in the study area.

Finally, there are still some uncertainties in such predictive approaches that are as follows; (1) inclusion of subsurface discontinuity network, spatially varying groundwater surface, and material heterogeneity in the 3D model, (2) inclusion of variable depth and phases in the runout modeling. Despite these possible uncertainties, which will be overcome in future prospects, such studies are required to minimize the risk and avert the possible disasters.

6 CONCLUSIONS

By utilizing field based data and numerical simulations of a massive (~9.1 Mm^2) 'Varlaam' landslide in the SE Carpathians (Romania), present study explored the potential response of this landslide in seismic and rainfall regime.

The slope revealed the Factor of Safety in a range of 1.09-1.32 along with a static displacement of 0.4-4 m that increases up to 8-60 m under seismic load. The Groundwater, implying the saturation, further decreased the slope stability owing to enhanced joint hydraulic pressure. Ground motion amplification, during seismic shaking, further revealed the potential instability of slope with a Peak Ground Acceleration (PGA) on the slope surface in a range of 0.65g - 1.88g. Such amplification pertains to complex topography of landslide, soil thickness variation, and impedance contrast.

Further, though the GW effect is obtained in the slope instability, potential response of the slope under excessive rainfall is also evaluated through debris flow runout analysis. The predicted debris flow revealed a non-linear increase in the debris flow height (9.0-26.0 m) and velocity (2.1-3.0 m/sec) along the river channel. This variation along the river channel is attributed to the river channel morphology and influx of debris flow material from the slope. Owing to the predictive nature of present study, the concept may be applied in other terrains subjected to frequent landslides mostly triggered by extreme rainfall & earthquakes.

Author contribution: VK and HBH conceived the idea. All authors participated in the field data collection & data interpretation. VK, LC, and ASM performed the numerical simulations. MM led the geomorphic interpretation. All authors contributed to the writing of the final draft.

Competing interests: The authors declare that they have no conflict of interest.

Financial support: Authors are thankful for the financial grant by the F.R.S.–FNRS Belgium in the frame of the Belgian-Swiss collaboration project ‘4D seismic response and slope failure’.

ACKNOWLEDGEMENT

Authors acknowledge Philippe Cerfontaine, Martin Depret, Nirmit Dhabaria and George Catalin Simion for data acquisition (DGPS and seismological measurements). VK is also thankful to Imlirenla Jamir for the constructive discussion related to hydrological parametres.

REFERENCES

Apostol, L.:The Mediterranean cyclones–the role in ensuring water resources and their potential of Apostol, L., 2008. The Mediterranean cyclones–the role in ensuring water resources and their potential of climatic risk, in the east of Romania. Present environment and sustainable development, 2, pp.143-163, 2008.

Asimaki, D. and Mohammadi, K.: On the complexity of seismic waves trapped in irregular topographies. Soil Dynamics and Earthquake Engineering, 114, 424-437, 2018.

Barton, N. and Choubey, V.:The shear strength of rock joints in theory and practice. Rock mechanics, 10(1), 1-54, 1977.

Barton, N. R.:A model study of rock-joint deformation, Int. J. Rock Mech. Min., 9, 579–602, 1972.

Bednarczyk, Z.: Identification of flysch landslide triggers using conventional and 'nearly real-time'monitoring methods–An example from the Carpathian Mountains, Poland. Engineering Geology, 244, 41-56, 2018.

Beguería, S., Van Asch, T.W., Malet, J.P. and Gröndahl, S.:A GIS-based numerical model for simulating the kinematics of mud and debris flows over complex terrain. Natural Hazards and Earth System Sciences, 9(6), pp.1897-1909, 2009.

Beresnev, I.A. and Wen, K.L.:Nonlinear soil response—A reality?. Bulletin of the Seismological Society of America, 86(6), pp.1964-1978, 1996.

Bhasin, R. and Kaynia, A.M.:Static and dynamic simulation of a 700-m high rock slope in western Norway. Engineering Geology, 71(3-4), pp.213-226, 2004.

Biggs, J.M. and Biggs, J.: Introduction to structural dynamics. McGraw-Hill College. 1964.

Bokelmann, G. and Rodler, F.A.:Nature of the Vrancea seismic zone (Eastern Carpathians)–New constraints from dispersion of first-arriving P-waves. Earth and Planetary Science Letters, 390, 59-68, 2014.

Bontemps, N., Lacroix, P., Larose, E., Jara, J. and Taipe, E.:Rain and small earthquakes maintain a slow-moving landslide in a persistent critical state. Nature communications, 11(1), pp.1-10, 2020.

Bouckovalas, G.D. and Papadimitriou, A.G.:Numerical evaluation of slope topography effects on seismic ground motion. Soil Dynamics and Earthquake Engineering, 25(7-10), 547-558, 2005.

Bourdeau, C. and Havenith, H.B.: Site effects modelling applied to the slope affected by the Suusamyr earthquake (Kyrgyzstan, 1992). Engineering Geology, 97(3-4), 126-145, 2008.

Cai, F. and Ugai, K.: Numerical analysis of rainfall effects on slope stability. International Journal of Geomechanics, 4(2), pp.69-78, 2004.

Cauchie, L., Mreyen, A.S., Micu, M., Cerfontaine, P. and Havenith, H.B.: Landslide characterization by seismic ambient noise analysis: application to Carpathian Mountains. In AGU Fall Meeting, DOI:10.13140/RG.2.2.18971.69924, 2019.

Chang, K.J. and Taboada, A.: Discrete element simulation of the Jiufengershan rock-and-soil avalanche triggered by the 1999 Chi-Chi earthquake, Taiwan. Journal of Geophysical Research: Earth Surface, 114(F3), 2009.

Chow, V.T.: Open-channel hydraulics. McGraw-Hill civil engineering series, 1959.

Christen, M., Kowalski, J. and Bartelt, P.:RAMMS: Numerical simulation of dense snow avalanches in three-dimensional terrain. Cold Regions Science and Technology, 63(1-2), 1-14, 2010.

Constantin, S., Bojar, A.V., Lauritzen, S.E. and Lundberg, J.:Holocene and Late Pleistocene climate in the sub-Mediterranean continental environment: A speleothem record from Poleva Cave (Southern Carpathians, Romania). Palaeogeography, Palaeoclimatology, Palaeoecology, 243(3-4), 322-338, 2007.

Coulomb, C. A.: An attempt to apply the rules of maxima and minima to several problems of stability related to architecture". Mémoires de l'Académie Royale des Sciences 7: 343-382, 1776.

Croitoru, A.E., Piticar, A. and Burada, D.C. :Changes in precipitation extremes in Romania. Quaternary International, 415, pp.325-335, 2016.

Cundall, P.A.: UDEC-A Generalised Distinct Element Program for Modelling Jointed Rock. Cundall (Peter) Associates Virginia Water (England), 1980.

Ding, M., Huang, T., Zheng, H. and Yang, G.:Respective influence of vertical mountain differentiation on debris flow occurrence in the Upper Min River, China. Scientific Reports, 10(1), 1-13, 2020.

Durand, V., Mangeney, A., Haas, F., Jia, X., Bonilla, F., Peltier, A., Hibert, C., Ferrazzini, V., Kowalski, P., Lauret, F. and Brunet, C.: On the link between external forcings and slope instabilities in the Piton de la Fournaise Summit Crater, Reunion Island. Journal of Geophysical Research: Earth Surface, 123(10), 2422-2442, 2018.

Fell, R. and Hartford, D.: Landslide risk management. Landslide risk assessment, 51, 109, 1997.

Fenton, G.A. and Griffiths, D.V.: Risk assessment in geotechnical engineering (Vol. 461). New York: John Wiley & Sons, 2008.

Froude, M.J. and Petley, D.N.: Global fatal landslide occurrence from 2004 to 2016. Natural Hazards and Earth System Sciences, 18(8), 2161-2181, 2018.

Gaudio, V.D., Zhao, B., Luo, Y., Wang, Y. and Wasowski, J.: Seismic response of steep slopes inferred from ambient noise and accelerometer recordings: the case of Dadu River valley, China. Engineering Geology, 259, 105197, 2019.

Gholamy, A. and Kreinovich, V.: Why Ricker wavelets are successful in processing seismic data: Towards a theoretical explanation. In 2014 IEEE Symposium on Computational Intelligence for Engineering Solutions (CIES) (pp. 11-16). IEEE, 2014.

Godt, J.W. and Coe, J.A.: Alpine debris flows triggered by a 28 July 1999 thunderstorm in the central Front Range, Colorado. Geomorphology, 84(1-2), 80-97, 2007.

Grecu, F., Zaharia, L., Ioana-Toroimac, G. and Armaș, I.: Floods and flash-floods related to river channel dynamics. In Landform dynamics and evolution in Romania (pp. 821-844). Springer, Cham., 2017.

Griffiths, D.V. and Lane, P.A.: Slope stability analysis by finite elements. Geotechnique, 49(3), 387-403, 1999.

Gupta, V., Jamir, I., Kumar, V., & Devi, M.: Geomechanical characterisation of slopes for assessing rockfall hazards in the Upper Yamuna Valley, Northwest Higher Himalaya, India. Himalayan Geology, 38(2), 156-170, 2017.

Haque, U., Da Silva, P.F., Devoli, G., Pilz, J., Zhao, B., Khaloua, A., Wilopo, W., Andersen, P., Lu, P., Lee, J. and Yamamoto, T.: The human cost of global warming: Deadly landslides and their triggers (1995–2014). Science of the Total Environment, 682, 673-684, 2019.

Hara, A., Ohta, T., Niwa, M., Tanaka, S. and Banno, T.: Shear modulus and shear strength of cohesive soils. Soils and Foundations, 14(3),1-12, 1974.

Havenith, H.B., Strom, A., Calvetti, F. and Jongmans, D.: Seismic triggering of landslides. Part B: Simulation of dynamic failure processes. Natural Hazards and Earth System Sciences, 3(6), 663-682, 2003.

Havenith, H.B., Torgoev, A., Braun, A., Schlögel, R. and Micu, M.: A new classification of earthquake-induced landslide event sizes based on seismotectonic, topographic, climatic and geologic factors. Geoenvironmental Disasters, 3(1), 1-24, 2016.

Helmstetter, A. and Garambois, S.: Seismic monitoring of Séchilienne rockslide (French Alps): Analysis of seismic signals and their correlation with rainfalls. Journal of Geophysical Research: Earth Surface, 115(F3), 2010.

Hoek, E. and Brown, E.T.: Practical estimates of rock mass strength. International journal of rock mechanics and mining sciences, 34(8), 1165-1186, 1997.

Hoek, E. and Diederichs, M.S.: Empirical estimation of rock mass modulus. International journal of rock mechanics and mining sciences, 43(2), 203-215, 2006.

Hoek, E., Carranza-Torres, C. and Corkum, B.: Hoek-Brown failure criterion-2002 edition. Proceedings of NARMS-Tac, 1(1), 267-273, 2002.

Huffman, G.J., Stocker, E.F., Bolvin, D.T., Nelkin, E.J. and Jackson T.: GPM IMERG Final Precipitation L3 1 day 0.1 degree x 0.1 degree V06, Edited by Andrey Savtchenko, Greenbelt, MD, Goddard Earth Sciences Data and Information Services Center (GES DISC), Accessed: Sep. 5, 2020, 10.5067/GPM/IMERGDF/DAY/06, 2019.

Hungr, O., Morgan, GC and Kellerhals, R.: Quantitative analysis of debris torrent hazards for design of remedial measures. Canadian Geotechnical Journal , 21 (4), 663-677, 1984.

Hungr, O.: A review of landslide hazard and risk assessment methodology. Landslides and engineered slopes. Experience, theory and practice, edited by: Aversa, S., Cascini, L., Picarelli, L., and Scavia, C., CRC Press, Boca Raton, FL, 3-27, 2018.

Hürlimann, M., Rickenmann, D., Medina, V. and Bateman, A.: Evaluation of approaches to calculate debris-flow parameters for hazard assessment. Engineering Geology, 102(3-4), 152-163, 2008.

Hutter, K., Svendsen, B. and Rickenmann, D.: Debris flow modeling: A review. Continuum mechanics and thermodynamics, 8(1), 1-35, 1994.

Ibs-von Seht, M. and Wohlenberg, J.: Microtremor measurements used to map thickness of soft sediments. Bulletin of the Seismological Society of America, 89(1), 250-259, 1999.

Ilinca, V.: Characteristics of debris flows from the lower part of the Lotru River basin (South Carpathians, Romania). Landslides, 11(3), 505-512, 2014.

Jakob, M., Hungr, O. and Jakob, D.M.: Debris-flow hazards and related phenomena (Vol. 739). Berlin: Springer., 2005.

Jamir, I., Gupta, V., Kumar, V. and Thong, G.T.: Evaluation of potential surface instability using finite element method in Kharsali Village, Yamuna Valley, Northwest Himalaya. Journal of Mountain Science, 14(8),1666-1676, 2017.

Jibson, R.: Summary of research on the effects of topographic amplification of earthquake shaking on slope stability. US Geological Survey, 87-269, 1987.

Jing, L.: A review of techniques, advances and outstanding issues in numerical modelling for rock mechanics and rock engineering. International Journal of Rock Mechanics and Mining Sciences, 40(3), 283-353, 2003.

Joyner, W. B., & Chen, A. T.: Calculation of nonlinear ground response in earthquakes. Bulletin of the Seismological Society of America, 65(5), 1315-1336, 1975.

Kahraman, S.: Evaluation of simple methods for assessing the uniaxial compressive strength of rock. International Journal of Rock Mechanics and Mining Sciences, 38(7), 981-994, 2001.

Klimeš, J., Rosario, A.M., Vargas, R., Raška, P., Vicuña, L. and Jurt, C.: Community participation in landslide risk reduction: a case history from Central Andes, Peru. Landslides, 16(9), 1763-1777, 2019.

Kuhlemeyer, R.L. and Lysmer, J.: Finite element method accuracy for wave propagation problems. Journal of Soil Mechanics & Foundations Div, 99(Tech Rpt), 1973.

Kumar, V., Gupta, V. and Jamir, I.: Hazard evaluation of progressive Pawari landslide zone, Satluj valley, Himachal Pradesh, India. Natural Hazards, 93(2), 1029-1047, 2018.

Kumar, V., Jamir, I., Gupta, V. and Bhasin, R.K.: Inferring potential landslide damming using slope stability, geomorphic constraints and run-out analysis; case study from the NW Himalaya. Earth Surface Dynamics, 9(2), 351-377, 2021.

Lenti, L., Martino, S.: The interaction of seismic waves with step-like slopes and its influence on landslide movements. Eng. Geol. 126, 19–36, 2012.

Li, B., Beaudoing, H. and Rodell, M. : GLDAS Catchment Land Surface Model L4 daily 0.25 x 0.25 degree GRACE-DA1 V2.2, Greenbelt, Maryland, USA, Goddard Earth Sciences Data and Information Services Center (GES DISC), Accessed: Sep. 5, 2020, 10.5067/TXBMLX370XX8, 2020.

Liang, W.L.: Dynamics of pore water pressure at the soil–bedrock interface recorded during a rainfall-induced shallow landslide in a steep natural forested headwater catchment, Taiwan. Journal of Hydrology, 587, 125003, 2020.

Lin, C.W., Liu, S.H., Lee, S.Y. and Liu, C.C.: Impacts of the Chi-Chi earthquake on subsequent rainfall-induced landslides in central Taiwan. Engineering Geology, 86(2-3), 87-101, 2006.

Liu, Z., Su, L., Zhang, C., Iqbal, J., Hu, B. and Dong, Z.: Investigation of the dynamic process of the Xinmo landslide using the discrete element method. Computers and Geotechnics, 123, p.103561, 2020.

Luo, Y., Fan, X., Huang, R., Wang, Y., Yunus, A.P. and Havenith, H.B.:Topographic and near-surface stratigraphic amplification of the seismic response of a mountain slope revealed by field monitoring and numerical simulations. Engineering Geology, 271, p.105607, 2020.

Magyari, E.K., Demény, A., Buczkó, K., Kern, Z., Vennemann, T., Fórizs, I., Vincze, I., Braun, M., Kovács, J.I., Udvardi, B. and Veres, D.: A 13,600-year diatom oxygen isotope record from the South Carpathians (Romania): Reflection of winter conditions and possible links with North Atlantic circulation changes. Quaternary International, 293, 136-149, 2013.

Margottini, C., Canuti, P. and Sassa, K.: Landslide science and practice (Vol. 1). Berlin: Springer, 2013.

Maţenco, L.: Tectonics and exhumation of Romanian Carpathians: inferences from kinematic and thermochronological studies. In Landform dynamics and evolution in Romania (pp. 15-56). Springer, Cham., 2017.

Matsui, T. and San, K.C.: Finite element slope stability analysis by shear strength reduction technique. Soils and foundations, 32(1), 59-70, 1992.

McCowan, D. W., & Lacoss, R. T.: Transfer functions for the seismic research observatory seismograph system. Bulletin of the Seismological Society of America, 68(2), 501-512, 1978.

McDowell, P.W.: The determination of the dynamic elastic moduli of rock masses by geophysical methods. Geological Society, London, Engineering Geology Special Publications, 6(1), 267-274, 1990.

McNally A.: FLDAS Noah Land Surface Model L4 Global Monthly 0.1 x 0.1 degree (MERRA-2 and CHIRPS), Greenbelt, MD, USA, Goddard Earth Sciences Data and Information Services Center (GES DISC), 10.5067/5NHC22T9375G, 2018.

Micu, M., Bălteanu, D., Micu, D., Zarea, R. and Raluca, R.: Landslides in the Romanian Curvature Carpathians in 2010. In Geomorphological impacts of extreme weather, Springer, Dordrecht, 251-264, 2013.

Micu, M., Jurchescu, M., Șandric, I., Mărgărint, C., Zenaida, C., Dana, M., Ciurean, R., Ilinca, V., Vasile, M.: Natural Risks - Mass Movements, in M. Radoane, A.Vespremeanu-Stroe (Eds.) Landform dynamics and evolution in Romania, Springer, 765-820, 2016.

Micu, M.: Landslide hazard assessment in Vrancea seismic region (Curvature Carpathians of Romania): achievements and perspectives. In 1st EAGE Workshop on Assessment of Landslide and Debris Flows Hazards in the Carpathians, 1-5, 2019.

Mihailovici, M., Gabor, O., Rândaşu, S., & Asman, I.: Floods in Romania. Hidrotehnica, 51(6), 23-35, 2006.

Mohr, O.: Abhandlungen aus dem Gebiete der Technischen Mechanik (2nd ed). Ernst, Berlin, 1914.

Mreyen, A.S., Cauchie, L., Micu, M., Onaca, A. and Havenith, H.B.: Multiple geophysical investigations to characterize massive slope failure deposits: application to the Balta rockslide, Carpathians. Geophysical Journal International, 225(2), 1032-1047, 2021.

Murgeanu, G., Dumitrescu, I., Sandulescu, M., Bandrabur, T. and Sandulesu, J.: Harta geologică a RS România. L-35-XXI, scara 1: 200.000, Foaia Covasna, 1965.

Murphy, J.R., Davis, A.H. and Weaver, N.L.: Amplification of seismic body waves by low-velocity surface layers. Bulletin of the Seismological Society of America, 61(1), 109-145, 1971.

Nakamura, Y.: Basic structure of QTS (HVSR) and examples of applications. In Increasing seismic Safety by combining engineering technologies and seismological data, Springer, Dordrecht., 33-51, 2009.

Novak, M. and Han, Y.C.: Impedances of soil layer with boundary zone. Journal of geotechnical engineering, 116(6), 1008-1014, 1990.

Obreht, I., Zeeden, C., Hambach, U., Veres, D., Marković, S.B., Bösken, J., Svirčev, Z., Bačević, N., Gavrilov, M.B. and Lehmkuhl, F.: Tracing the influence of Mediterranean climate on Southeastern Europe during the past 350,000 years. Scientific Reports, 6(1), 1-10, 2016.

O'Brien, J.S., Julien, P.Y. and Fullerton, W.T.: Two-dimensional water flood and mudflow simulation. Journal of hydraulic engineering, 119(2), 244-261, 1993.

Peranić, J., Moscariello, M., Cuomo, S. and Arbanas, Ž.: Hydro-mechanical properties of unsaturated residual soil from a flysch rock mass. Engineering Geology, 269, 105546, 2020.

Petrescu, L., Stuart, G., Tataru, D. and Grecu, B.: Crustal structure of the Carpathian Orogen in Romania from receiver functions and ambient noise tomography: how craton collision, subduction and detachment affect the crust. Geophysical Journal International, 218(1), 163-178, 2019.

Pollock, W. and Wartman, J.: Human vulnerability to landslides. Geohealth, 4(10), p.e2020GH000287, 2020.

Pospíšil, L., Hefty, J. and Hipmanová, L.: Risk and geodynamically active areas of the Carpathian lithosphere on the base of geodetical and geophysical data. Acta Geodaetica et Geophysica Hungarica, 47(3), 287-309, 2012.

Radulian, M., Bonjer, K.P., Popa, M. and Popescu, E.: Seismicity patterns in SE Carpathians at crustal and subcrustal domains: tectonic and geodynamic implications. In Proceedings of the International Symposium on Strong Vrancea Earthquakes and Risk Mitigation, Bucharest, Romania, 4-6, 2007.

Remaître, A., Malet, J.P. and Maquaire, O. : Morphology and sedimentology of a complex debris flow in a clay-shale basin. Earth surface processes and landforms, 30(3), 339-348, 2005.

Rickenmann, D. and Scheidl, C.: Debris-flow runout and deposition on the fan. In Dating torrential processes on fans and cones, Springer, Dordrecht,75-93, 2013.

Ricker, N.: Further developments in the wavelet theory of seismogram structure. Bulletin of the Seismological Society of America, 33(3), 197-228, 1943.

Şafak, E.:Local site effects and dynamic soil behavior. Soil Dynamics and Earthquake Engineering, 21(5), 453-458, 2001.

Salm, B.: Flow, flow transition and runout distances of flowing avalanches. Annals of Glaciology, 18, 221-226, 1993.

Sassa, K.: ISDR-ICL Sendai Partnerships 2015–2025 for global promotion of understanding and reducing landslide disaster risk. Landslides, 12(4), 631-640, 2015.

Shieh, C.L., Chen, Y.S., Tsai, Y.J. and Wu, J.H.: Variability in rainfall threshold for debris flow after the Chi-Chi earthquake in central Taiwan, China. International Journal of Sediment Research, 24(2), 177-188, 2009.

Simoni, A., Bernard, M., Berti, M., Boreggio, M., Lanzoni, S., Stancanelli, L.M. and Gregoretti, C.: Runoff-generated debris flows: Observation of initiation conditions and erosion–deposition dynamics along the channel at Cancia (eastern Italian Alps). Earth Surface Processes and Landforms, 45(14), 3556-3571, 2020.

Tang, C., Zhu, J., Qi, X. and Ding, J.: Landslides induced by the Wenchuan earthquake and the subsequent strong rainfall event: A case study in the Beichuan area of China. Engineering Geology, 122(1-2), 22-33, 2011.

Tischler, M., Matenco, L., Filipescu, S., Gröger, H.R., Wetzel, A. and Fügenschuh, B.: Tectonics and sedimentation during convergence of the ALCAPA and Tisza–Dacia continental blocks: the Pienide nappe emplacement and its foredeep (N. Romania). Geological Society, London, Special Publications, 298(1), 317-334, 2008.

Ustaszewski, K., Schmid, S.M., Fügenschuh, B., Tischler, M., Kissling, E. and Spakman, W.: A map-view restoration of the Alpine-Carpathian-Dinaridic system for the Early Miocene. Swiss Journal of Geosciences, 101(1), 273-294, 2008.

Van Asch, T.W., Buma, J. and Van Beek, L.P.H.: A view on some hydrological triggering systems in landslides. Geomorphology, 30(1-2), 25-32, 1999.

Van Westen, C.J., Van Asch, T.W. and Soeters, R.: Landslide hazard and risk zonation—why is it still so difficult? Bulletin of Engineering geology and the Environment, 65(2), 167-184, 2006.

Voellmy, A.: Über die Zerstörungskraft von Lawinen. Schweiz. Bauztg, 1955.

Wang, G., Suemine, A. and Schulz, W.H.: Shear-rate-dependent strength control on the dynamics of rainfall-triggered landslides, Tokushima Prefecture, Japan. Earth Surface Processes and Landforms, 35(4), 407-416, 2010.

Witherspoon, P.A., Wang, J.S., Iwai, K. and Gale, J.E.: Validity of cubic law for fluid flow in a deformable rock fracture. Water resources research, 16(6), 1016-1024, 1980.

LIST OF FIGURES AND TABLES

Fig. 1: Study area. Inset ‘a’ (source: NOAA/NCEI, USA) ‘b’ (after Ustaszewski et al. 2008) highlight the position of study area. Geological setting and Paleo-landslides locations are based on Murgeanu et al. 1965; Tischler et al. 2012; Pospisil and Hipmanova 2012.

Fig. 2: Landslide features. (a) Landslide marked with different features, (b) Crown portion, (c) Right flank, (d) Left flank, (e) Signs of failure in the flow deposits. Image Source: Google Earth.

Fig. 3: Rainfall (RF), Soil Moisture (SM), and Surface Runoff (RF) pattern. The region in which these parametres are extracted has been highlighted in Fig. 1. Dataset (except Fig. 3j) source: FLDAS_NOAH01_C_GL_M model (McNally et al. 2018). Spatial resolution of dataset: 0.1° (~10 km). Data source of Fig. 3j: GPM IMERG Final Precipitation (Huffman et al. 2019). Spatial resolution of dataset: 0.1°. The rainfall data in Fig. 3j is available only from 1 June, 2000. The SM and SR data is not available at daily scale for the study area. Blue line (in Fig. a, d, g) indicates linear regression and shaded region around it refers to 95% confidence interval. Dots in box plots refer to outliers. Red line in Fig. 3j refers to extreme rainfall (30mm/24 h). Grey shaded region in Fig. 3k refer to those months that witnessed above average values of RF, SM, and SR.

Fig. 4: Earthquake pattern. (a-b) Position of study area (c) Depth and Earthquake magnitude (d) Distance of epicentres from landslide and Earthquake magnitude. Blue line (in Fig. 4d) indicates linear regression and shaded region around it refers to 95% confidence interval. Data source: National Institute for Earth Physics, Romania.

Fig. 5: Landslide model construction. (a) Measured peak frequency distribution. Based on Cauchie et al. 2019, (b) Digital elevation model, (c) Soil (or debris) thickness pattern in the landslide, (d) Cross sectional view of landslide model.

Fig. 6: Model configuration for the Slope stability analysis. (a) Landslide model. The location of the different cross sections used in the UDEC models are marked by red lines, (b-e) Configuration of the sections; CS-1 to CS-4.

Fig. 7: Seismic signals in time & frequency domain. (a &b) Ricker Wavelet (as recorded at the model base monitoring point) (c & d) 1976 Friuli Earthquake, (Italy). Note: Different time scale.

Fig. 8: Factor of Safety (FS) and material displacement (X-direction). a – d refer to original slope sections with sub-sections (red rectangle) used to represent displacement. e –h, i-l, m-p, and q-t refer to displacement in static, static +GW, dynamic, and dynamic +GW conditions, respectively.

Fig. 9: Comparison of material displacement under different conditions. St. and Dy. refer to Static and Dynamic conditions, respectively. GW refers to Groundwater.

Fig. 10: Parametric analysis. (a-d) Variation in the FS, (e-h) Variation in the static displacement, (i-l) Variation in the dynamic displacement. Grey bar represents the values that are used in the slope stability analysis (sec. 4.1). Notably, vertical axes in 'e-l' are kept same to show relative increase in displacement under static and dynamic conditions.

Fig. 11: Maximum acceleration at different monitoring points.

Fig. 12: Spectral ratio pattern. (a) CS-2 model with the position of monitoring points. (b) Spectral ratio pattern in the CS-2, (c) CS-3 model with the position of monitoring points, (d) Spectral ratio pattern in the CS-3.

Fig. 13: Debris flow run-out pattern. (a) Soil (or debris) thickness pattern in the landslide, (b) Different release area depths (5, 10, 15, and 20 m) used for the analysis (c) River profile section A-B used to represent the resultant debris flow along the river, (d-f) results at 5 m depth, (g-i) results at 10 m depth, (j-l) results at 15 m depth, (m-o) results at 20 m depth.

Fig. 14: Relationship of channel width and debris flow characteristics (a-c) and results of sensitivity analysis at constant 'maximum' friction and variable turbulence (d-f). The 'Ups and Dws' refer to Upstream and Downstream side of the river channel.

Fig. 15: Debris flow run-out pattern at 20 m depth. (a) Upstream view of landslide from the right flank, (b) Run-out pattern at 20 m depth, (c) Top view of landslide highlighting two regions where runout reached across the river (d) Runout pattern near left flank extending across the river channel, (e) Runout pattern near right flank extending across the river channel.

Table 1: Input parameters used in the slope stability analysis.

Table 2: Input parameters used in the Run-out simulation

Table 3: Results of the Run-out simulation at different depths of release area.

Table 1: Input parameters used in the slope stability analysis.

Rockmass parameters	values	Rockmass-soil interface (shear horizon) parameters	values	Soil parameters	value
Density, γ (Gg/m^3)	0.0025	[4]Normal Stiffness, k_n (MPa/m)	~10000	Density, γ (Gg/m^3)	0.0019
[1]Uniaxial Compressive Strength, σ_{ci} (MPa)	~30	Shear Stiffness , k_s (k_n/10) MPa/m	~1000	[2]Poisson's Ratio	~0.43
[2]Poisson's Ratio	~0.4	[5]Cohesion, c (MPa)	~0.01	[2]Young's Modulus, E (MPa)	549± 38
[2]Young's Modulus, E (MPa)	3658± 1411	[6]Friction angle, Ø	~30°	[2]Bulk Modulus, K (MPa)	1316± 206
[2]Bulk Modulus, K (MPa)	7308± 4014	[7]Residual aperture at high stress, m	0.0001	[2]Shear Modulus, G (MPa)	194± 14
[2]Shear Modulus, G (MPa)	1303± 480	[7]Aperture for zero normal stress, m	0.0005	[5]Cohesion, c (MPa)	~0.01
[3]GSI	30	Water density, Gg/m^3	0.001	[5]Friction angle, Ø	~28°
[3]Material Constant (m_i)	17± 4	[7]Joint permeability, (1/MPa*s)	10^8		
m_b	1.3954				
s	0.004				
a	0.5223				
[3]D	0				

[1]It was inferred from the empirical equation of Kahraman (2001) using the Vs and Vp data of Mreyen et al. (2021).
[2]These values were inferred from the empirical equations of McDowell (1990) using the P & S wave velocity of Mreyen et al. (2021).
[3]Based on Hoek and Brown (1997) and field observation.
[4]It was inferred from from the empirical equations of Barton (1972); Hoek and Diederichs (2006) using the elastic modulus of rock and approximated spacing of joint sets of~5-10cm. This spacing was assumed in view of highly sheared nature of rockmass.
[5]Based on Bednarczyk (2018); Peranić et al. (2020) due to similar litho- tectonic conditions.
[6]Based on Barton and Choubey (1977).
[7]Based on UDEC v.6 (2014).

Table 2: Input parameters used in the Run-out simulation

Landslide	Material type	Material depth[1], m	Friction coefficient[2]	Turbulence coefficient[3], m/sec^2
Varlaam	Clayey Silt	5, 10, 15, 20	μ= 0.4	ξ = 250

[1] Considering that fact that during slope failure, irrespective of type of trigger, entire loose material might not slide down, the depth is taken as a variable.[2] In order to keep the results of conservative nature, we have taken a maximum allowable friction i.e., μ= 0.4 (Hungr et al., 1984; RAMMS v.1.7.0). This case is considered to understand the potential impacts of debris flow even after the maximum friction. [3]This range is used in view of the type of loose material i.e., cohesive (RAMMS v.1.7.0).

Table 3: Results of the Run-out simulation at different depths of release area.

Release area depth, m	**At hillslope**		**Along the river channel**	
	Maximum flow height, m	Maximum flow velocity, m/s	Maximum flow height, m	Maximum flow velocity, m/s
5	8.0	4.5	9.0	3.0
10	20.0	10.0	16.0	2.9
15	30.0	16.0	22.0	2.2
20	42.0	21.0	26.0	2.1

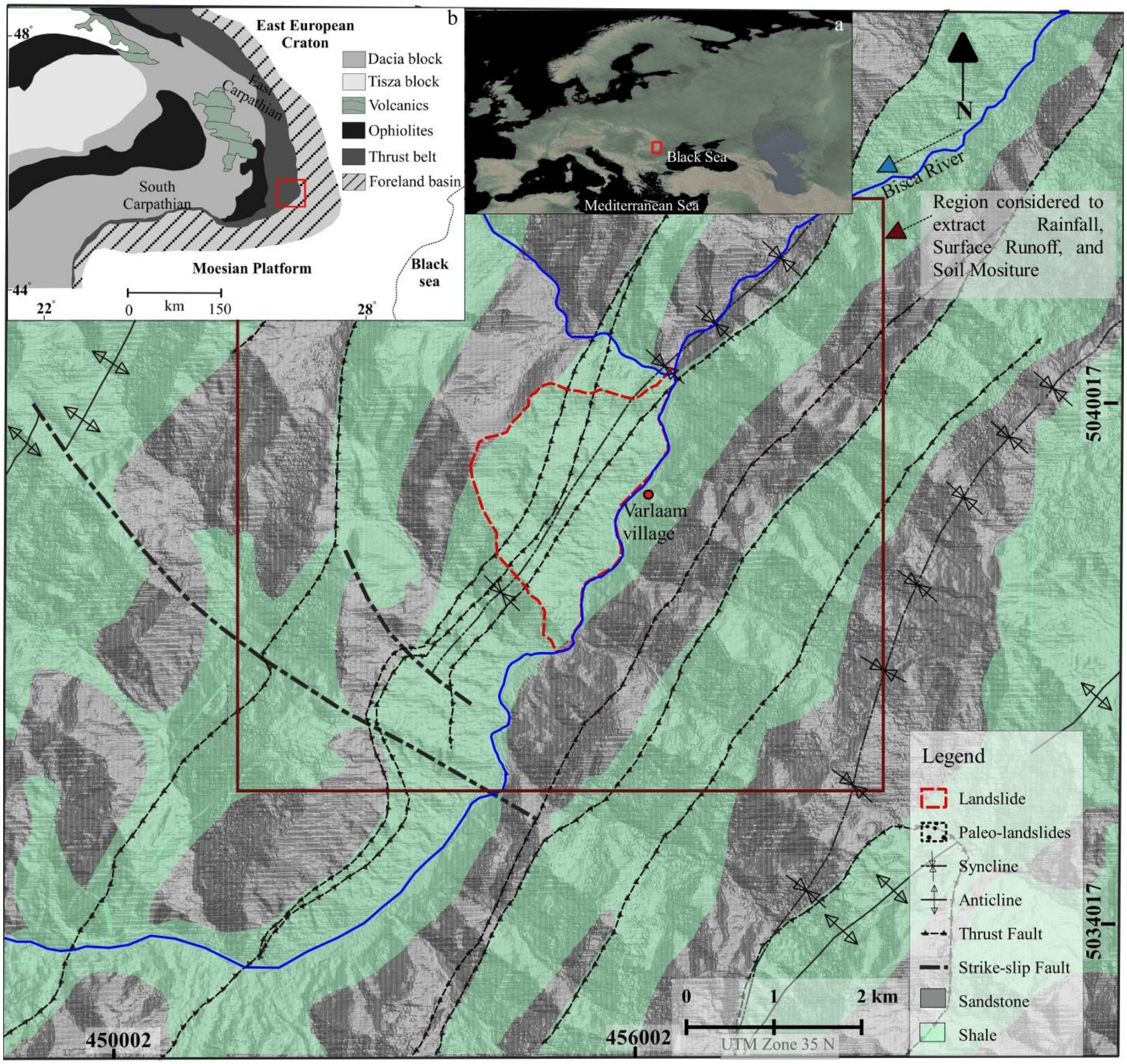
East European Craton
b
48°
Dacia block
Tisza block
Volcanics
Ophiolites
Thrust belt
Foreland basin
East Carpathian
South Carpathian
Moesian Platform
Black sea
44°
22°
0
km
150
28°
a
Black Sea
Mediterranean Sea
N
Bisca River
Region considered to extract Rainfall, Surface Runoff, and Soil Mositure
Varlaam village
5040017
5034017
Legend
Landslide
Paleo-landslides
Syncline
Anticline
Thrust Fault
Strike-slip Fault
Sandstone
Shale
0
1
2 km
UTM Zone 35 N
450002
456002

Fig. 1


a
Crown
b
Left flank
d
c
e
Right flank
1 km
Google Earth
Image © 2021 CNES / Airbus
Image © 2021 Maxar Technologies
b
Paleo-detachment depression
N
500 m
c
N
Seasonal flow channel/gully
500 m
Google Earth
Image © 2021 Maxar Technologies
d
e
100 m
N
Relics of paleo-flow/slide movements
500 m

Fig. 2

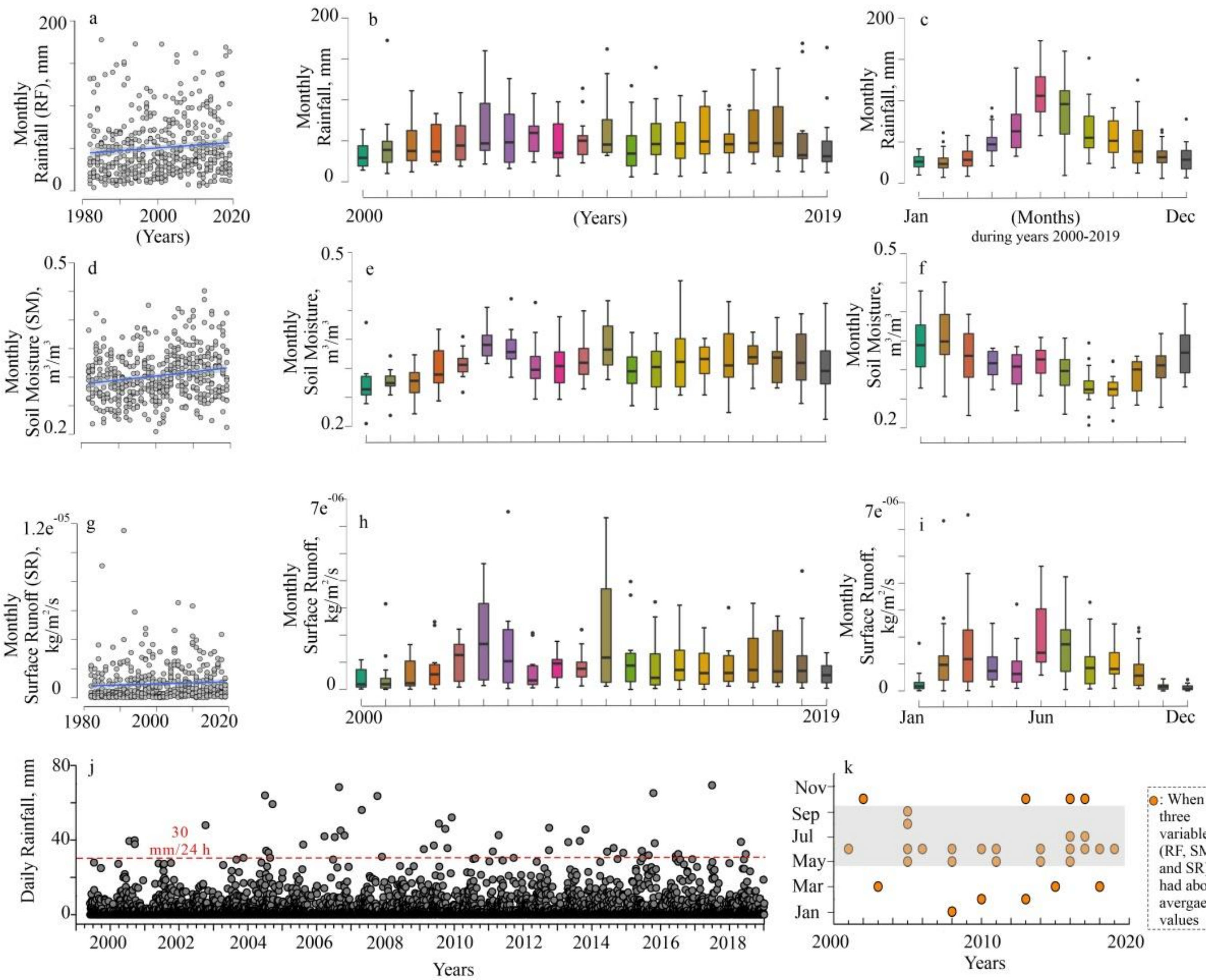
a
Monthly Rainfall (RF), mm
(Years)
b
Monthly Rainfall, mm
(Years)
c
Monthly Rainfall, mm
(Months)
during years 2000-2019
d
Monthly Soil Moisture (SM), m³/m³
e
Monthly Soil Moisture, m³/m³
f
Monthly Soil Moisture, m³/m³
g
Monthly Surface Runoff (SR), kg/m²/s
h
Monthly Surface Runoff, kg/m²/s
i
Monthly Surface Runoff, kg/m²/s
j
Daily Rainfall, mm
30 mm/24 h
Years
k
Years
: When all three variables (RF, SM, and SR) had above avergae values

Fig. 3

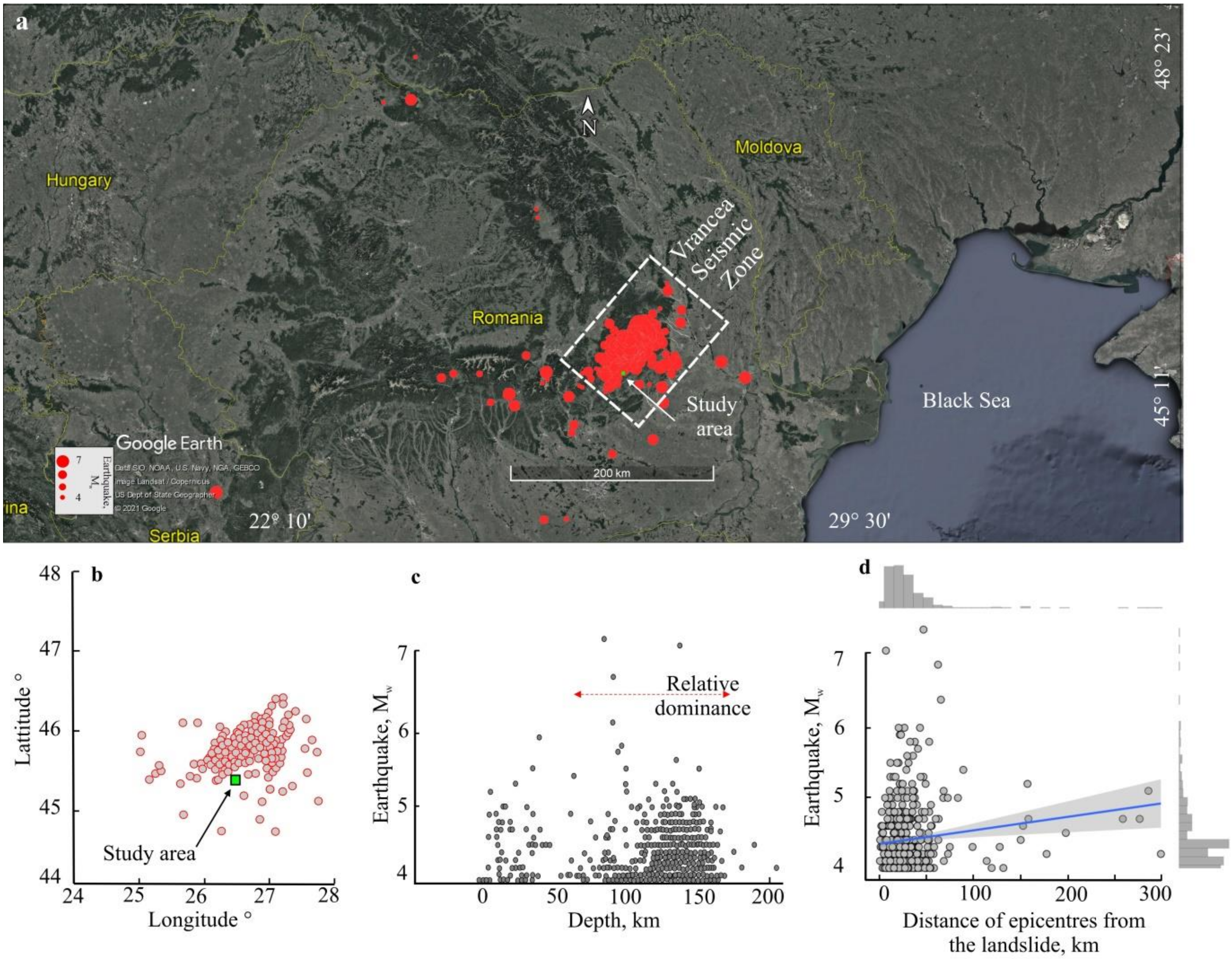
a
48° 23'
N
Hungary
Moldova
Vrancea
Seismic
Zone
Romania
Study
area
Black Sea
45° 11'
Google Earth
200 km
Earthquake, M_w
7
4
Data SIO, NOAA, U.S. Navy, NGA, GEBCO
Image Landsat / Copernicus
US Dept of State Geographer
© 2021 Google
22° 10'
29° 30'
Serbia
b
Lattitude °
Longitude °
Study area
c
Earthquake, M_w
Relative
dominance
Depth, km
d
Earthquake, M_w
Distance of epicentres from
the landslide, km

Fig. 4

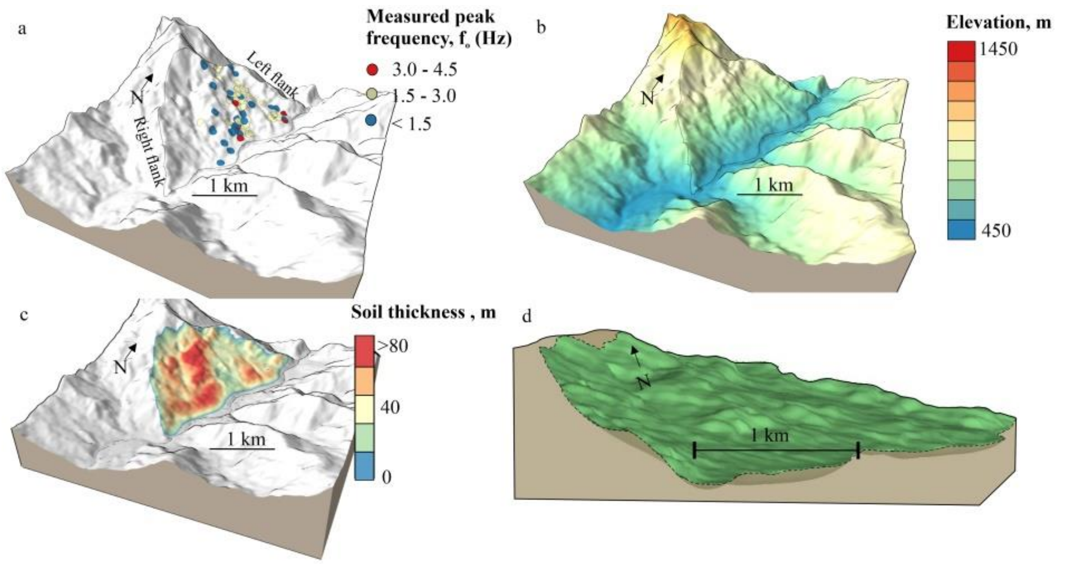
a
Measured peak frequency, f_o (Hz)
3.0 - 4.5
1.5 - 3.0
< 1.5
Left flank
Right flank
N
1 km
b
Elevation, m
1450
450
N
1 km
c
Soil thickness , m
>80
40
0
N
1 km
d
N
1 km

Fig. 5

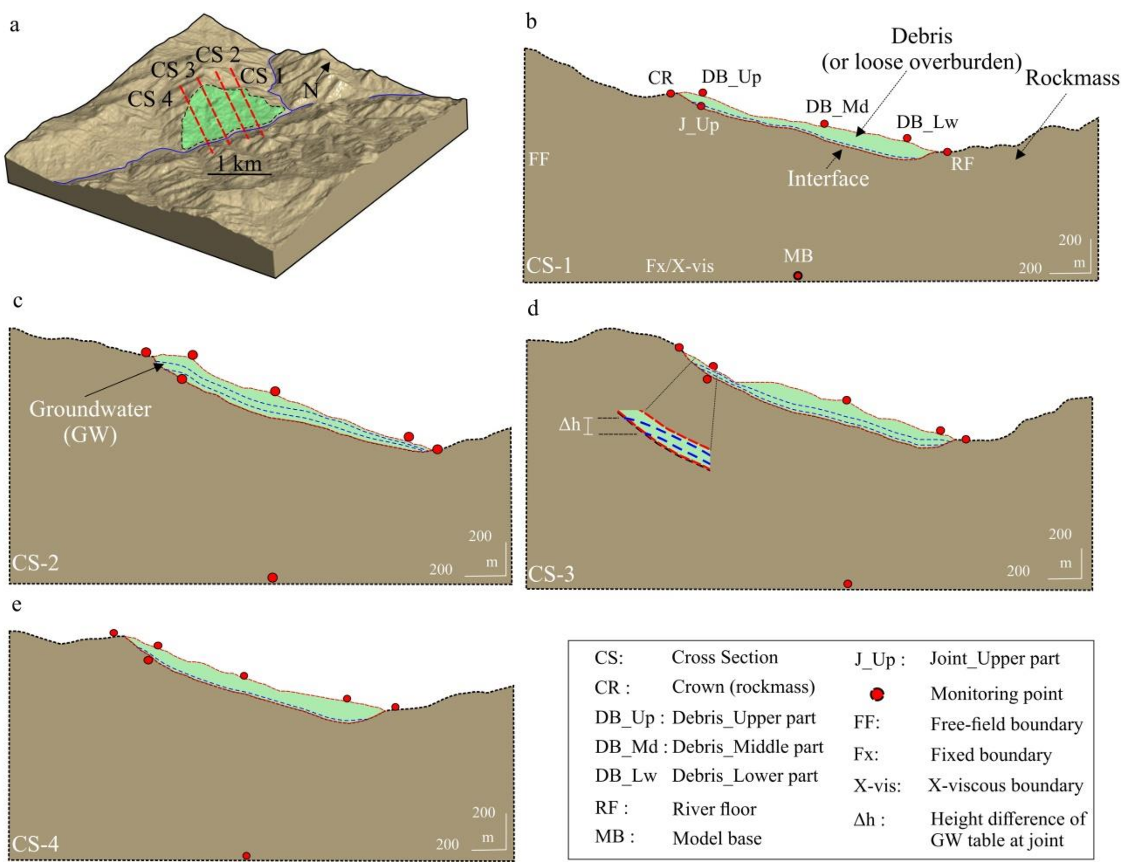
a
CS 3
CS 2
CS 1
CS 4
N
1 km
b
Debris
(or loose overburden)
Rockmass
CR
DB_Up
J_Up
DB_Md
DB_Lw
RF
FF
Interface
CS-1
Fx/X-vis
MB
200
200
m
c
Groundwater
(GW)
CS-2
200
200
m
d
Δh
CS-3
200
200
m
e
CS-4
200
200
m
CS: Cross Section
CR : Crown (rockmass)
DB_Up : Debris_Upper part
DB_Md : Debris_Middle part
DB_Lw Debris_Lower part
RF : River floor
MB : Model base
J_Up : Joint_Upper part
Monitoring point
FF: Free-field boundary
Fx: Fixed boundary
X-vis: X-viscous boundary
Δh : Height difference of GW table at joint

Fig. 6

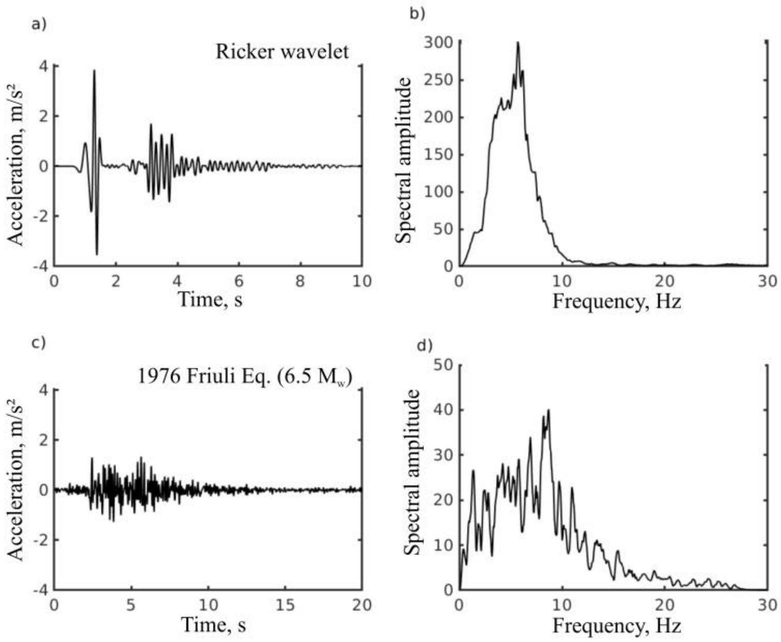
a)
Ricker wavelet
Acceleration, m/s²
Time, s
b)
Spectral amplitude
Frequency, Hz
c)
1976 Friuli Eq. (6.5 M_w)
Acceleration, m/s²
Time, s
d)
Spectral amplitude
Frequency, Hz

Fig. 7

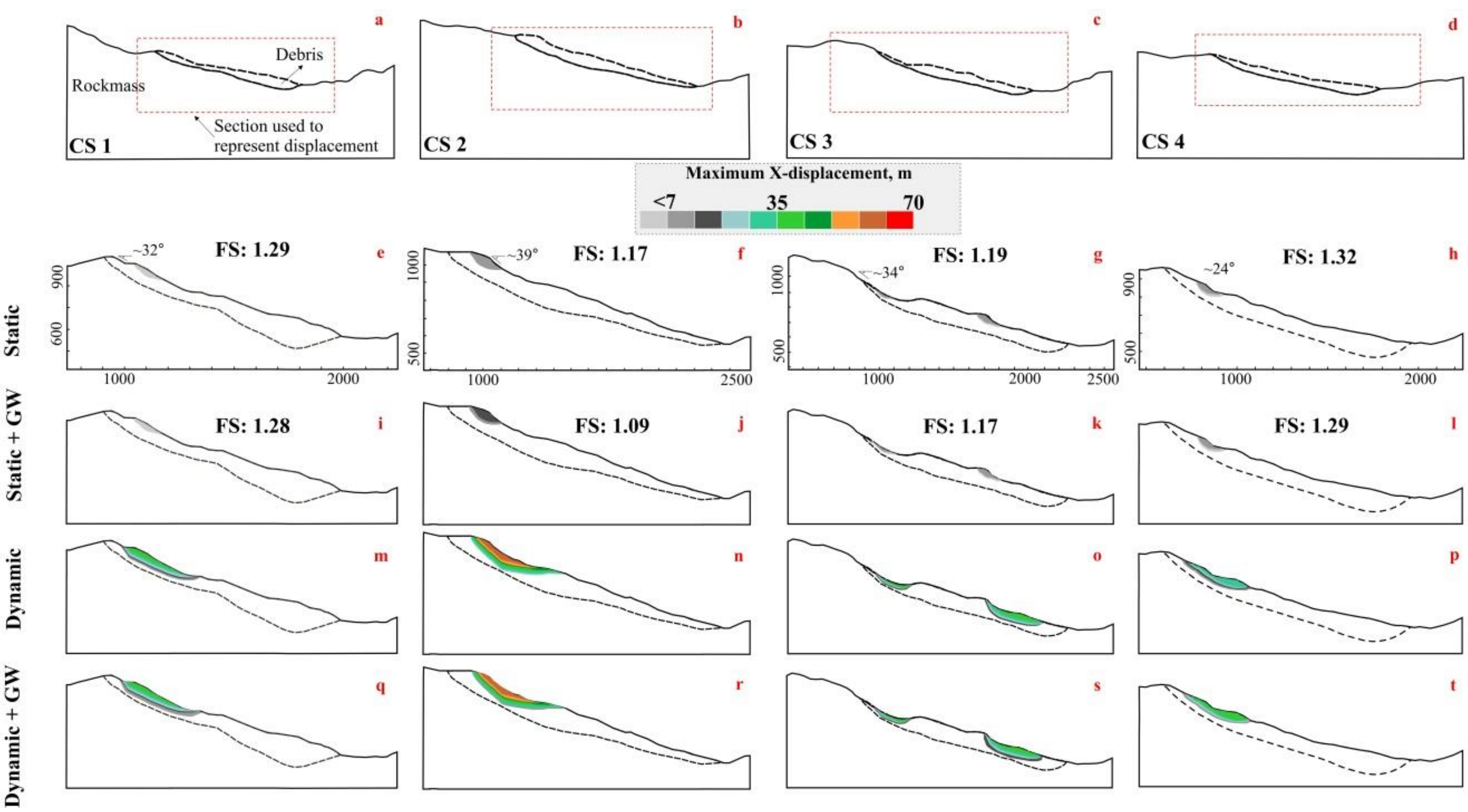
Rockmass
Debris
Section used to represent displacement
CS 1
CS 2
CS 3
CS 4
Maximum X-displacement, m
<7
35
70
FS: 1.29
FS: 1.17
FS: 1.19
FS: 1.32
FS: 1.28
FS: 1.09
FS: 1.17
FS: 1.29
~32°
~39°
~34°
~24°
Static
Static + GW
Dynamic
Dynamic + GW

Fig. 8

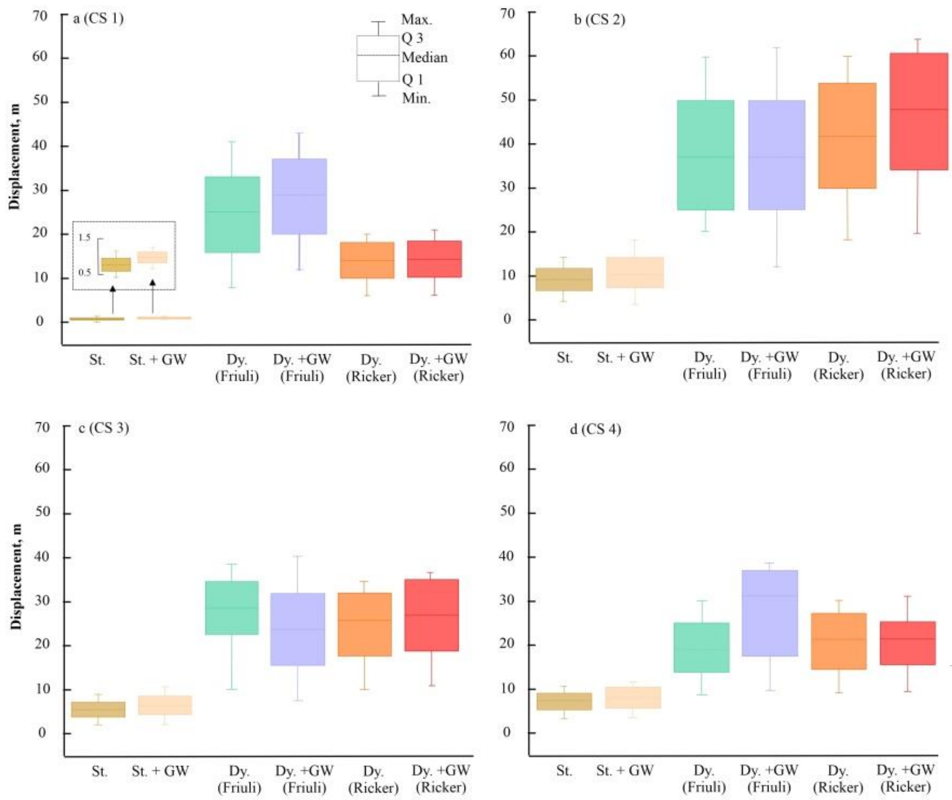

a (CS 1)
b (CS 2)
c (CS 3)
d (CS 4)
Max.
Q 3
Median
Q 1
Min.
Displacement, m
St.
St. + GW
Dy. (Friuli)
Dy. +GW (Friuli)
Dy. (Ricker)
Dy. +GW (Ricker)

Fig. 9

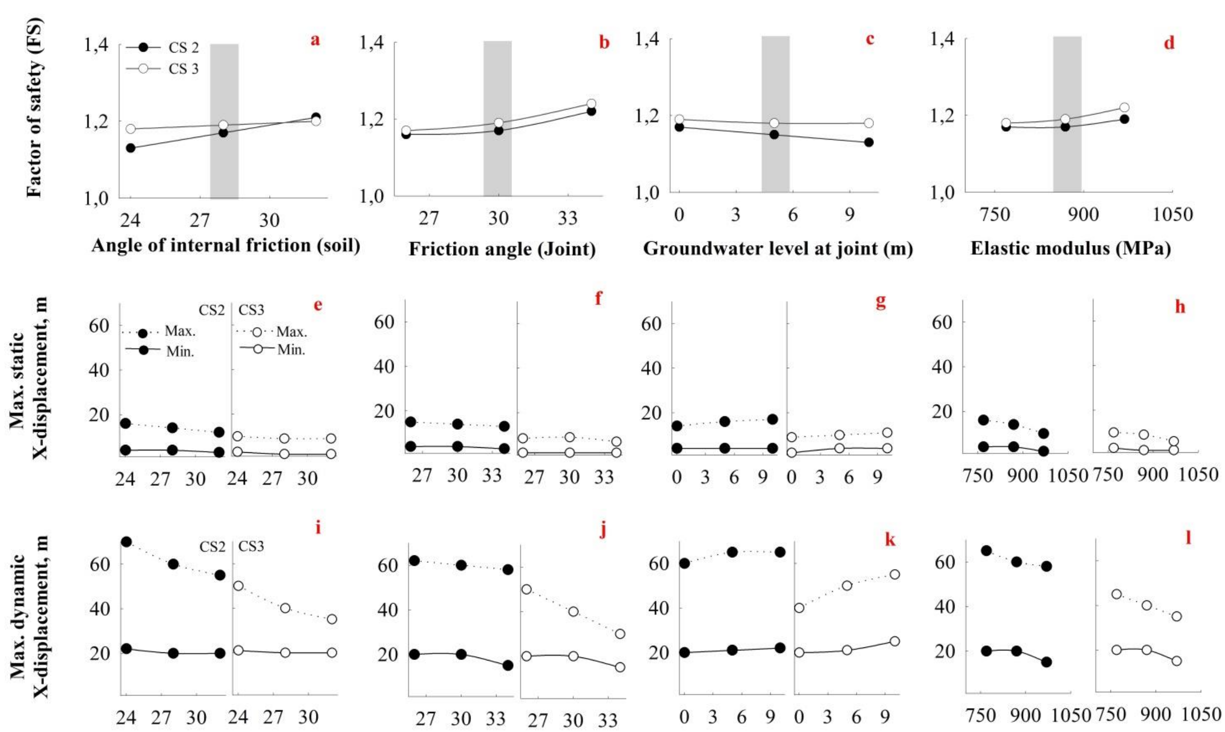

Factor of safety (FS)
CS 2
CS 3
Angle of internal friction (soil)
Friction angle (Joint)
Groundwater level at joint (m)
Elastic modulus (MPa)
Max. static X-displacement, m
Max. dynamic X-displacement, m
Max.
Min.
CS2
CS3

Fig. 10

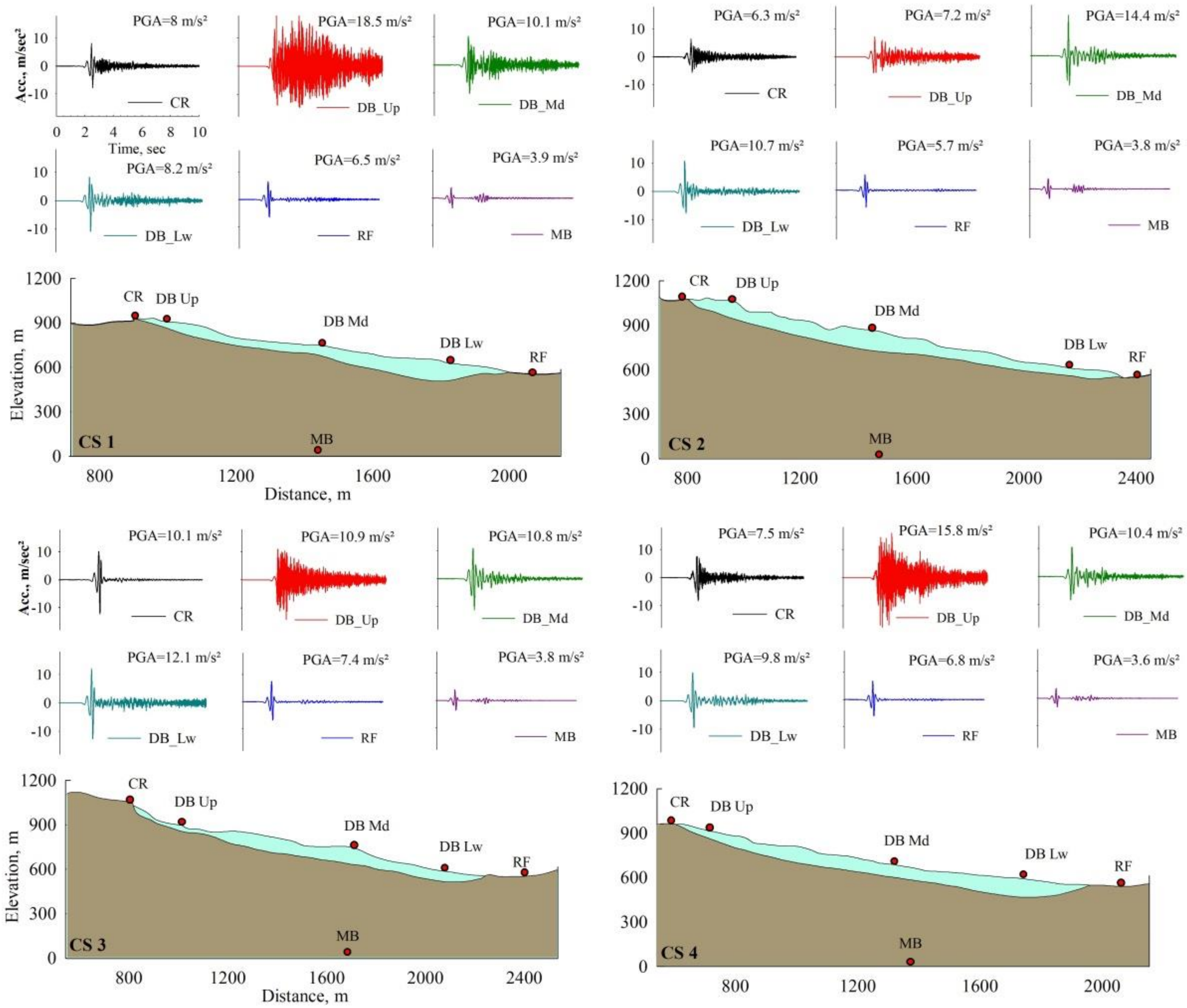

PGA=8 m/s²
PGA=18.5 m/s²
PGA=10.1 m/s²
CR
DB_Up
DB_Md
Acc., m/sec²
Time, sec
PGA=8.2 m/s²
PGA=6.5 m/s²
PGA=3.9 m/s²
DB_Lw
RF
MB
PGA=6.3 m/s²
PGA=7.2 m/s²
PGA=14.4 m/s²
PGA=10.7 m/s²
PGA=5.7 m/s²
PGA=3.8 m/s²
CS 1
CS 2
Elevation, m
Distance, m
DB Up
DB Md
DB Lw
PGA=10.1 m/s²
PGA=10.9 m/s²
PGA=10.8 m/s²
PGA=12.1 m/s²
PGA=7.4 m/s²
PGA=3.8 m/s²
PGA=7.5 m/s²
PGA=15.8 m/s²
PGA=10.4 m/s²
PGA=9.8 m/s²
PGA=6.8 m/s²
PGA=3.6 m/s²
CS 3
CS 4

Fig. 11

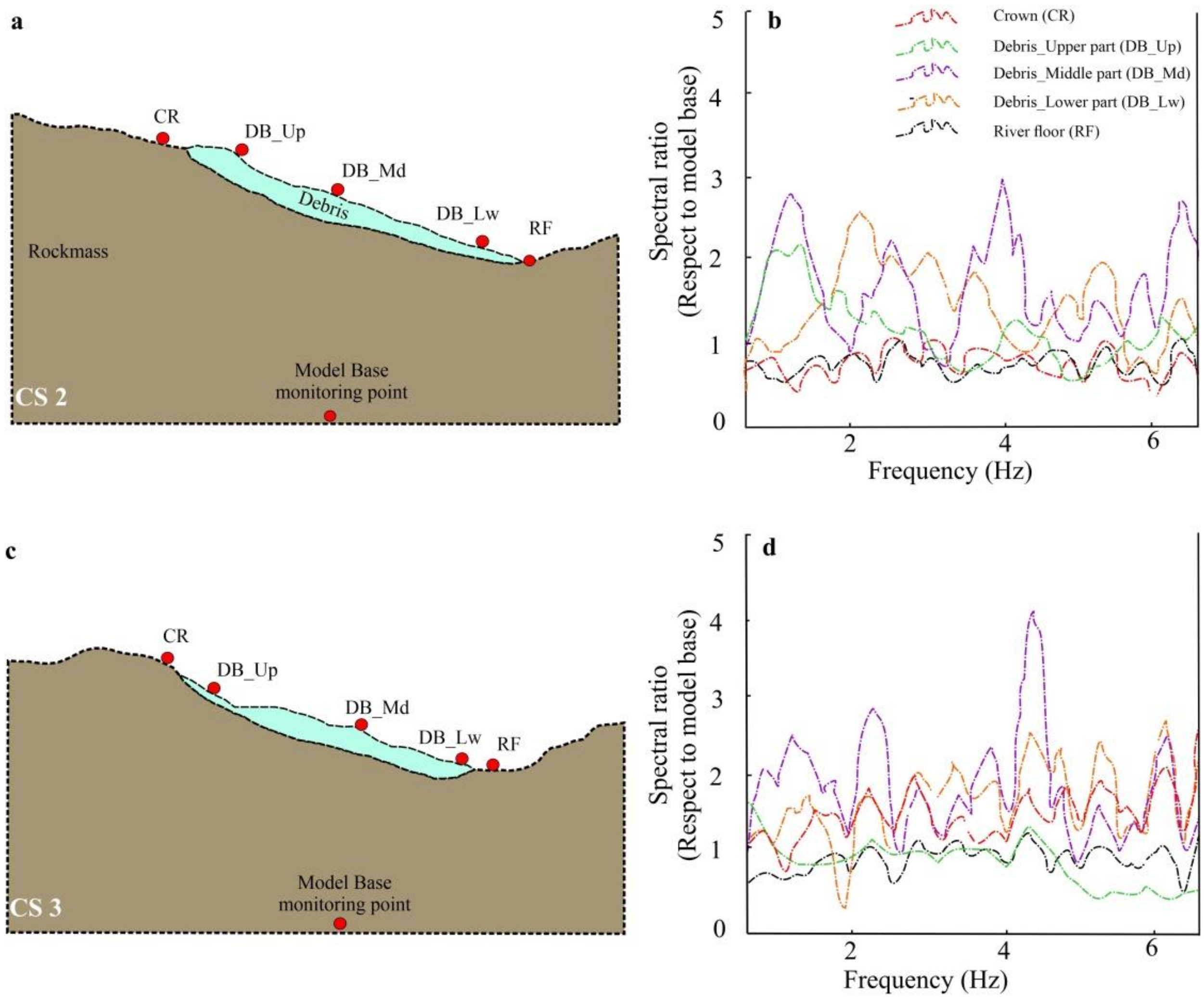
a
CR
DB_Up
DB_Md
Debris
DB_Lw
RF
Rockmass
Model Base
monitoring point
CS 2
b
Crown (CR)
Debris_Upper part (DB_Up)
Debris_Middle part (DB_Md)
Debris_Lower part (DB_Lw)
River floor (RF)
Spectral ratio
(Respect to model base)
Frequency (Hz)
c
CR
DB_Up
DB_Md
DB_Lw
RF
Model Base
monitoring point
CS 3
d
Spectral ratio
(Respect to model base)
Frequency (Hz)

Fig. 12

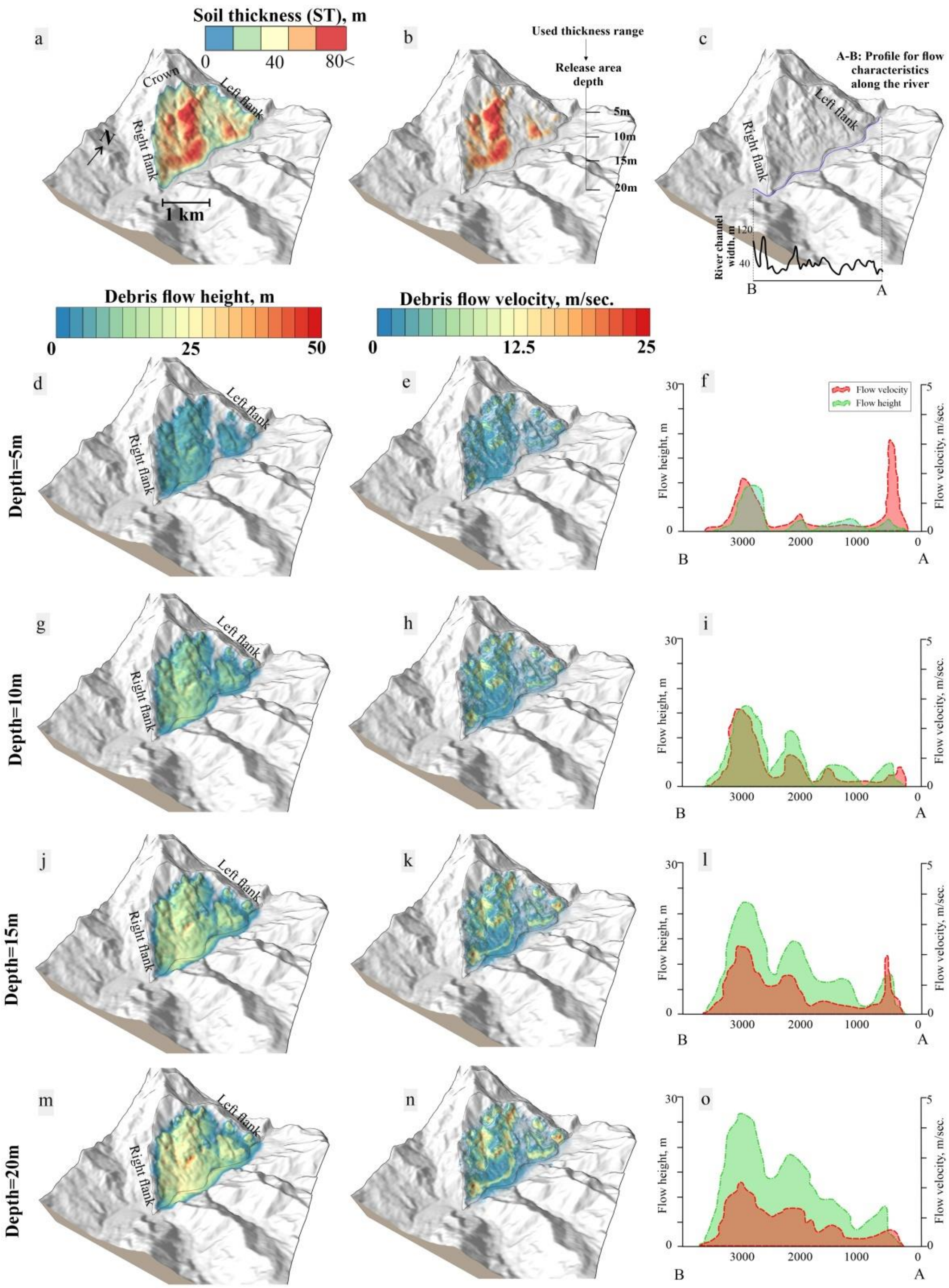

Soil thickness (ST), m
0
40
80<
Crown
Left flank
Right flank
N
1 km
Used thickness range
Release area depth
5m
10m
15m
20m
A-B: Profile for flow characteristics along the river
River channel width, m
120
40
B
A
Debris flow height, m
0
25
50
Debris flow velocity, m/sec.
0
12.5
25
Depth=5m
Depth=10m
Depth=15m
Depth=20m
Flow velocity
Flow height
Flow height, m
Flow velocity, m/sec.
3000
2000
1000

Fig. 13

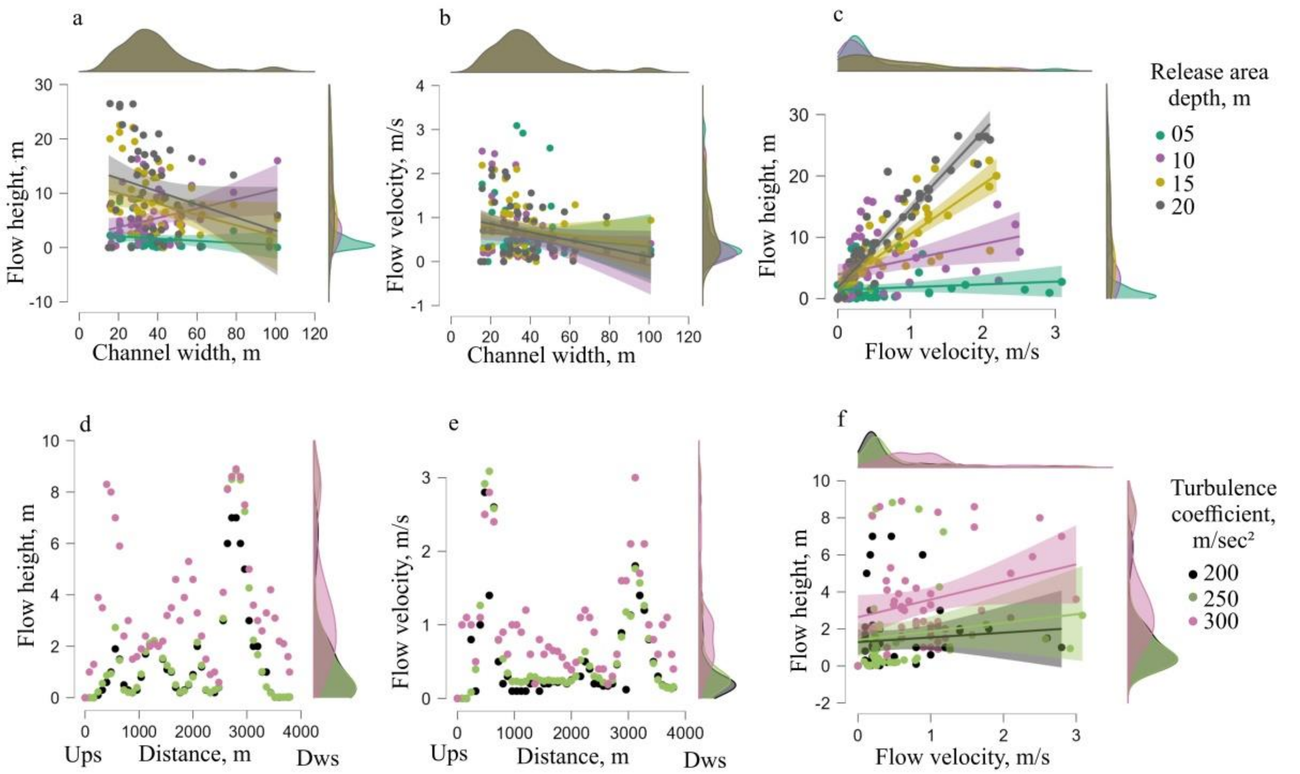

a
b
c
Flow height, m
Channel width, m
Flow velocity, m/s
Release area depth, m
05
10
15
20
d
e
f
Distance, m
Ups
Dws
Turbulence coefficient, m/sec²
200
250
300

Fig. 14

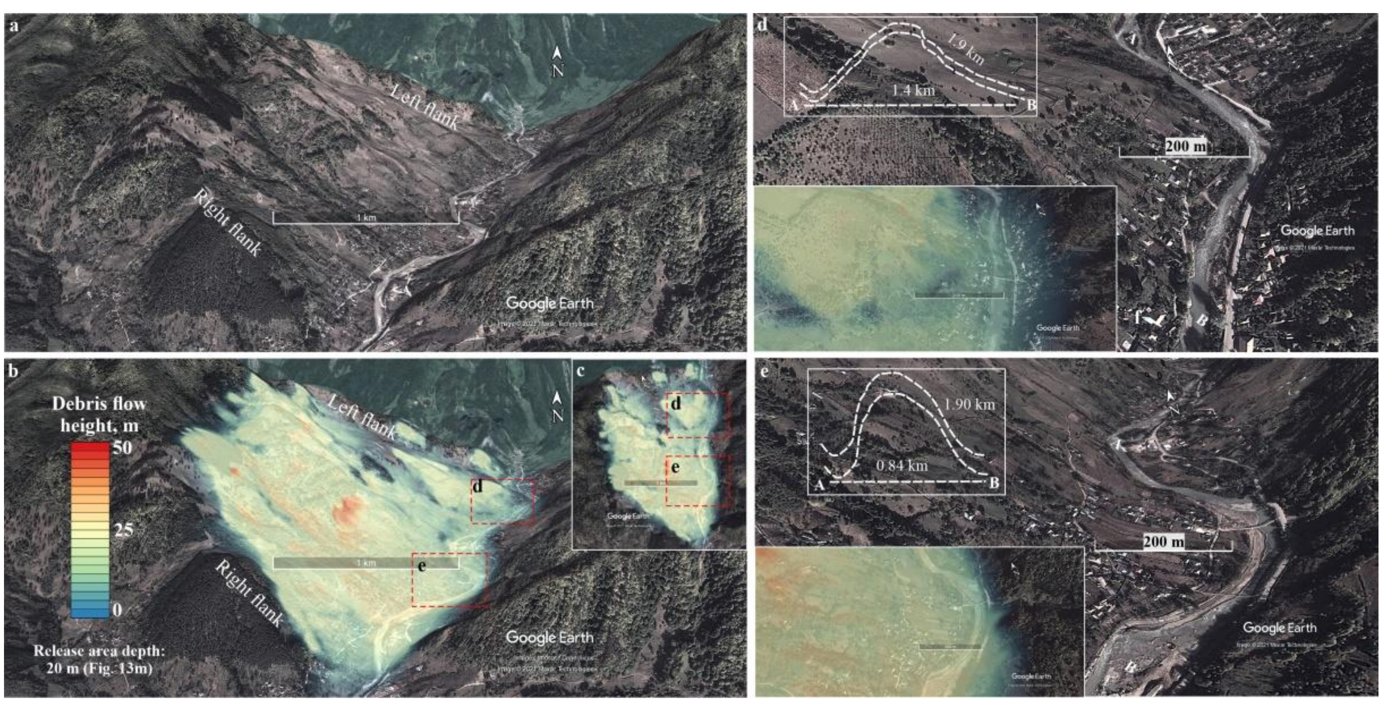

Left flank
Right flank
1 km
Google Earth
1.9 km
1.4 km
A
B
200 m
Debris flow height, m
50
25
0
Release area depth: 20 m (Fig. 13m)
1.90 km
0.84 km

Fig. 15